2022-05-01

Material Synthesis and Machine Learning for Additive Manufacturing

Jaime Eduardo Regis
The University of Texas at El Paso

MATERIAL SYNTHESIS AND MACHINE LEARNING FOR ADDITIVE MANUFACTURING

JAIME EDUARDO REGIS

Doctoral Program in Mechanical Engineering

APPROVED:

Yirong Lin, Ph.D., Chair

Tzu-Liang Tseng, Ph.D.

Angel Flores Abad, Ph.D.

Sabrina Torres, Ph.D.

Stephen L. Crites, Jr., Ph.D.
Dean of the Graduate School

Dedication

To the people that have supported me at every step of the way, especially those who could not be with us at the end of the journey.

MATERIAL SYNTHESIS AND MACHINE LEARNING FOR ADDITIVE MANUFACTURING

by

JAIME EDUARDO REGIS, B.A.

DISSERTATION

Presented to the Faculty of the Graduate School of

The University of Texas at El Paso

in Partial Fulfillment

of the Requirements

for the Degree of

DOCTOR OF PHILOSOPHY

Department of Aerospace & Mechanical Engineering

THE UNIVERSITY OF TEXAS AT EL PASO

May 2022

Acknowledgements

I would like to acknowledge my friends and family for all of their love and support. I would also like to thank the LSAMP program faculty for helping me during my early years of the doctoral program and teaching me the skills I needed to be successful.

Additionally, I would like to express gratitude to my committee chair, Dr. Yirong Lin for his guidance and for always pushing me seize opportunities presented to me. I would also like to thank my committee members, Dr. Tzu-Lian Tseng, Dr. Angel Flores Abad, and Dr. Sabrina Torres for offering insightful feedback to ensure success in my dissertation.

Lastly, I would like to thank all of my Elsa Bramasco, Andrea Irigoyen, Sebastian Vargas, Christian Ruiz and Cesar Dominguez for their friendship and hard work over the years. I would also like to thank my peer Anabel Renteria for always challenging me and helping me improve my research.

Abstract

The goal of this research was to address three key challenges in additive manufacturing (AM), the need for feedstock material, minimal end-use fabrication from lack of functionality in commercially available materials, and the need for qualification and property prediction in printed structures. The near ultraviolet-light assisted green reduction of graphene oxide through L-ascorbic acid was studied with to address the issue of low part strength in additively manufactured parts by providing a functional filler that can strengthen the polymer matrix. The synthesis of self-healing epoxy vitrimers was done to adapt high strength materials with recyclable properties for compatibility with AM technology. Lastly, machine vision and machine learning were used for the autonomous characterization of micro and macrostructure and performance prediction in syntactic foams and lattice structures.

Table of Contents

List of Tables

List of Figures

Chapter 1: Introduction

1.1 Motivation

With the increasing demand for tailored made parts, additive manufacturing (AM) has quickly been gaining interest for materials processing. AM enables the freedom of geometrical design, customization with no added cost from traditional manufacturing methods, and fabrication of complex geometries by taking a computer designed structure and slicing it into individual layer that can then be deposited by a variety of methods[1]. The lower cost of manufacturing, rapid prototyping, fabrication of complex geometry and custom building has given AM technology a competitive edge over traditional methods in the manufacturing of materials. However, there are several challenges that need to be addressed for the technology to progress beyond its use as a rapid prototyping tool or simply an intermediary step[2]. These challenges include lack of feedstock material that is compatible with the technology, minimal end-use fabrication due to the lack of high strength or functional materials, and the need for qualification and property prediction. Through this dissertation, the issues in additive manufacturing are addressed with the use of functional fillers such as graphene, the adaptation of novel materials such as vitrimers for compatibility with the technology, and the qualification of AM fabricated parts through machine vision and machine learning.

1.2 Background

1.2.1 Graphene

One of the methods to mitigate the low part strength of printed polymers is through the use of functional filler such as graphene. Graphene has been a highly regarded material since 2004 when co-workers Konstantin Novoselov and Andre Geim employed a simple mechanical a simple mechanical exfoliation technique to obtain single layered graphene[3]. Graphene's high

modulus of elasticity[4], thermal conductivity[5], and electron mobility[6] have enabled its use in various applications including high-end composite materials[4,7,8],sensors[9–11], electronics[12,13], and energy storage devices[14–16]. Additionally, its optical transmittance[17,18] and high surface area[19] make graphene an ideal material for energy collection devices[20,21]. Several methods have been developed over the years to produce graphene including mechanical exfoliation[22–24], chemical vapor deposition[25–27], and liquid phase exfoliation[28–30]. When incorporated into a polymer matrix, graphene has the capability to improve the mechanical properties while adding electrical and thermal conductivity functionalities[31].

1.2.2 Covalent adaptive network polymers

Polymers are generally divided into two categories, thermoplastics and thermosets, based on the bonds that form between the polymer chains[32]. Thermoplatics are formed by physical bonds that although weak, allow for reprocessibility and recyclability. Thermosets, on the other hand, have strong covalent bonds that give the polymer high strength, resistance to chemical solvents, and heat stability. In recent years, polymers with the strength of thermosets and reprocessability of thermoplastics, known as covalent adaptive networks (CANs), have been gaining increasing interest. CANs can be described as polymer networks with dynamic crosslinks that are capable of reconfiguring their network topology and reform broken bonds through intricate chemical processes[33]. Various CANs have been continuously adapted for their use in additive manufacturing (AM) to mitigate negative effects of the printing process[34] such as improving inter filament adhesion and therefore strength[35] or by allowing materials that would otherwise not be processable through AM to be compatible with the technology[36–38].

1.2.3 Machine learning/vision for advanced manufacturing

The lack of qualification and property prediction of 3D printed parts is a challenge in AM which is being addressed through the use of machine learning. Machine learning is a series of procedures and algorithms that analyze data to recognize patterns, clusters, or trends for the extraction of useful information[39]. In AM, process parameters are obtained through loops of trial-and-error, a repetitive process which is largely dependent on the capabilities of an operator to recognize anomalies and make the corresponding adjustment[40]. However, these patterns can often be difficult to notice for which machine learning can easily draw inferences. Machine learning has been applied at various steps of the additive manufacturing process being used for design optimization prior to printing[41,42], quality assurance and defect detection in conjunction with machine vision during the printing process[43,44], and for performance prediction of the printed part after the process[45].

Chapter 2: Green reduction of graphene oxide through near-ultraviolet light and l-ascorbic acid

2.1 Introduction

Graphene has many desirable properties such as high modulus of elasticity[4], thermal conductivity[5], and electron mobility[6] that can be passed down to a polymer matrix when used as a nanofiller. Nevertheless, these production methods of graphene are associated with either high cost of production or low scalability which limit the use of graphene in commercial applications[46]. Consequently, one of the more well-studied methods of recent years has been the reduction of graphene oxide (GO) due to its scalability[24,47,48] and tunability[49,50]. GO is typically synthesized by oxidizing graphite using a strong acid mixture such as potassium chlorate ($KClO_3$) with nitric acid (HNO_3) as described by the Brodie and Staudenmaier methods[51], or by using potassium permanganate ($KMnO_4$) with sulfuric acid (H_2SO_4) in the more commonly used Hummer's method[52–54]. The produced multilayered GO is then subjected to liquid exfoliation by sonication in water or organic solvents to produce single-layered GO[55]. In order to remove oxygen functionalities and obtain a product with comparable properties to graphene, GO is reduced by various means[56], although primarily through a chemical reduction process[57,58].

As an efficient chemical reductant, hydrazine has been the most widely used, but its toxicity and adverse effects on the environment[59,60] have prompted a search for green alternatives such as plant extracts[61–63], microorganisms[64–66], sugars[67], proteins[68,69], and organic acids[70]. While these alternatives are much safer for the environment, the quality of the reduced graphene oxide produced, as characterized by various chemical structural characterization methods, cannot yet reproduce the quality of reduced GO produced from using hydrazine[71]. However, few alternatives including l-ascorbic acid[72], glucose[73], starch-

based materials[74], hydrogen rich water[75], ginseng[76], natural cellulose[77], backer's yest[78], and gallic acid[79], amongst others[80–85], have shown reduction efficiencies comparable to hydrazine.

Recently, L-ascorbic acid (L-AA), an organic acid, has demonstrated its potential to be a green, low cost, substitute to hydrazine due to its anti-oxidative properties and abundance. The reduction of GO through L-AA has been demonstrated to occur at room temperature[86]; however, conditions such as alkaline pH, high L-AA to GO ratio, and applied heating can increase the rate of reduction from 48 hours, to nearly under one hour. In addition, stirring and sonication have also been shown to affect the rate of reduction as well as the quality of the reduced product[87].

Previous studies have shown that L-AA is highly photosensitive[88], and as such, relevant parameters such as radiation type, wavelength and power of light source could be used to directly affect the effectiveness of L-AA as a green reducing agent for graphene oxide. In this study, the effects NUV light on the reductive behavior of green reductant L-AA in GO films are investigated. Our wide-angle x-ray scattering (WAXS) analysis after 48-hour exposure to L-AA, shows that GO films exhibit variable degrees of reduction depending on the length of exposure to L-AA, as it is revealed by the detection of two distinct peaks, corresponding to the c-lattice spacing of two distinct structural phases within the films. X-ray photoelectron spectroscopy (XPS) and Fourier transform infrared (FT-IR) spectroscopy were also used to further analyze the degree of reduction and provide evidence that chemical methods under external stimuli can prove to be effective at obtaining metastable reduced graphene oxide films, in comparison to previous reports[89]. Additionally, NUV-radiation was shown to assist in preventing the films from redispersing in the aqueous solution by making them hydrophobic in the surface. As a result, the films can be immersed in aqueous solutions for longer periods without the risk of resuspension.

2.2 Experimental Details

2.2.1 Materials

Graphene oxide in a 5 mg/mL suspension was purchased from Goographene (Virginia, United States). L-ascorbic acid (99% purity) was obtained from Sigma Aldrich (Darmstadt, Germany). Graphene oxide (GO) films were prepared by drop-casting 15 mL of GO solution onto a quartz glass substrate and dried overnight in air at room temperature. An aqueous solution composed of 5 g of L-ascorbic acid (L-AA) and 20 mL of deionized (DI) water, based on a previous report[90], was carefully pipetted onto the GO films and left soaking for different time periods. GO films in L-AA solution were irradiated by a 405 nm wavelength near ultraviolet (NUV) light using a FormCure from Formlabs (Massachusetts, United States) for different lengths, 1 hour, 2 hours, and 3 hours. After the L-AA solution and NUV light exposure, films were washed and neutralized with DI water to remove the L-AA from the films. GO films were then left to dry overnight in air at room temperature.

2.2.2 Synthesis and fabrication

The drop-casting method produced uniform graphene oxide (GO) films (Figure 2.2.2: Digital images of graphene oxide film (a) drop casted on quartz glass substrate and (b) film immediately after chemical reduction through L-AA.); however, due to the hydrophilic properties of GO, special care was given to the samples when immersed in L-AA solution and when washed to avoid agitation that would lead to the films breaking apart from resuspension or redispersion. NUV-irradiated films and films with longer (over four hours) L-AA exposure demonstrated higher integrity in the aqueous solution than the controlled GO films and films with one, two, and three hours of exposure to L-AA solution, which is an indication of higher degree of reduction considering the hydrophobic nature of reduced graphene[91,92].

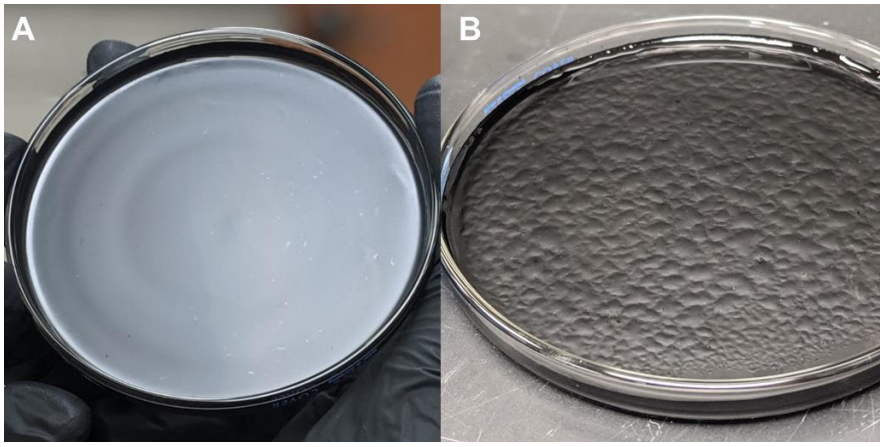

Figure 2.2.2: Digital images of graphene oxide film (a) drop casted on quartz glass substrate and (b) film immediately after chemical reduction through L-AA.

2.2.3 Material characterization

The thickness and surface morphology of GO films were characterized through scanning electron microscopy (SEM) on a thermionic ISM-IT500 from JEOL (Massachusetts, United States) under high vacuum, 10.0 kV accelerating voltage using a secondary electron detector. The efficiency of NUW exposure in the removal of oxygen-containing groups was analyzed through Fourier transform infrared spectroscopy (FT-IR) using a Cary 630 FT-IR spectrometer from Agilent (California, United States). Wide-angle x-ray scattering (WAXS) measurements were carried out using a Xenoc Xeuss 2.0 HR SAXS/WAXS system (Sassenage, France) with a Cu source tuned to λ = 0.1542 nm. In WAXS, x-rays scattered as a function of the scattering angle 2θ with respect to the transmitted direct beam were collected on the detector. The 2-D data was azimuthally averaged and plotted as I(Q). Here, Q is given by equation 1,

$$Q = \frac{4\pi \sin\theta}{\lambda} \tag{1}$$

where θ is half the scattering angle and λ is the wavelength of the source beam. I(Q) was scaled to units of differential scattering cross section per unit volume (cm^{-1}) using a glassy

carbon intensity calibration standard[93]. To ensure that samples produced isotropic scattering when hit by the x-ray beam, films were crushed into a fine powder and vacuum dried (Supplementary Section). Furthermore, the interlayer spacing, d, for the GO samples was calculated using Bragg's law (equation 2[94],

$$d = \frac{\lambda}{2\sin\theta} \tag{2}$$

X-ray photoelectron spectroscopy (XPS) was performed on an AXIS ULTRA X-Ray Photoelectron Spectrometer from Kratos (Manchester, United Kingdom). In order to acquire representative data for the entire film, samples were ground up into a powder and multiple readings were taken from different locations.

2.3 Results and Discussion

2.3.1 Microstructure

The thickness of the GO films were estimated from their cross-sectional view (Figure 2.3.1: Scanning electron micrographs of graphene oxide films treated with l-ascorbic acid and near ultraviolet light displaying folds on the surface (A and B). Cross-sectional micrographs of the film reveal waviness in a stacked structure.A) at multiple locations through scanning electron microscopy (SEM). An average film thickness of 2.89 ± 0.14 μm was measured. This cross-section of the GO films revealed a tightly packed, layered structure formed by graphene oxide laminates. Furthermore, small pockets can be observed in treated samples (Figure 2.3.1: Scanning electron micrographs of graphene oxide films treated with l-ascorbic acid and near ultraviolet light displaying folds on the surface (A and B). Cross-sectional micrographs of the film reveal waviness in a stacked structure.B) likely due to partial intercalation of water and L-AA solution in the inner GO stackings without complete delamination.

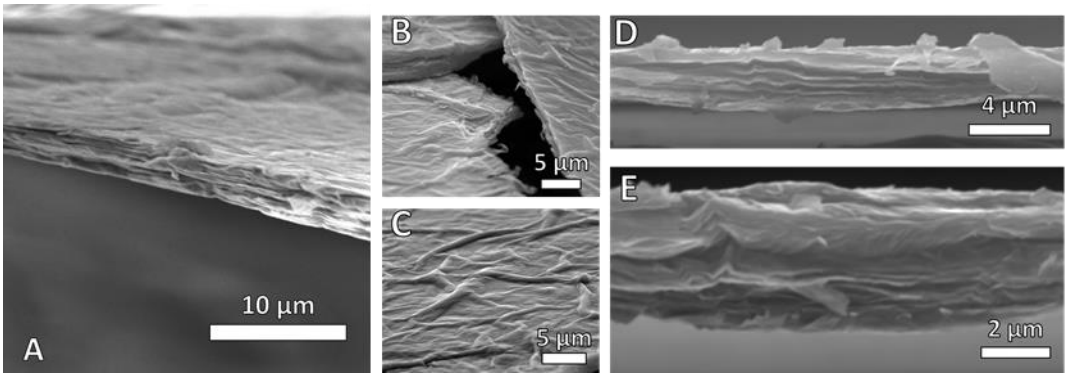

Figure 2.3.1: Scanning electron micrographs of graphene oxide films treated with l-ascorbic acid and near ultraviolet light displaying folds on the surface (A and B). Cross-sectional micrographs of the film reveal waviness in a stacked structure.

From the micrographs of the film's surface (Figure 2.3.1: Scanning electron micrographs of graphene oxide films treated with l-ascorbic acid and near ultraviolet light displaying folds on the surface (A and B). Cross-sectional micrographs of the film reveal waviness in a stacked structure.C), wrinkles and folds averaging a width of 1.73 µm and varying lengths can be seen throughout the film. These wrinkles are caused by drying and are prominent in graphene oxide films after the evaporation of water from the drop-casting procedure [95–97].

2.3.2 Fourier transform infrared spectroscopy

Graphene oxide peaks located at 1029 cm-1 (C-O stretching), 1262 cm-1 (C-OH bending), 1340 cm-1 (O-H bending), 1616 cm-1 (C=C stretching), 1728 cm-1 (C=O stretching), and 3116 cm-1 (O-H stretching) were observed (Figure 2.3.2: Fourier transform infrared spectrum for graphene oxide films comparing NUV-irradiated with unirradiated after one hour (A), two hours (B), three hours (C), and four hours (D) of exposure to l-ascorbic acid.). Samples soaked in L-AA solution for one hour (Figure 2.3.2: Fourier transform infrared spectrum for graphene oxide films comparing NUV-irradiated with unirradiated after one hour (A), two hours (B), three hours (C), and four hours (D) of exposure to l-ascorbic acid.A). did not show

significant differences between NUV-irradiated and unirradiated GO. The presence of the narrow band of OH vibration further suggest the presence of intercalated water in the films. Flattening of this band was observed to occur within two hours in irradiated samples (Figure 2.3.2: Fourier transform infrared spectrum for graphene oxide films comparing NUV-irradiated with unirradiated after one hour (A), two hours (B), three hours (C), and four hours (D) of exposure to l-ascorbic acid.B) while the same feature was not observed in unirradiated samples until three hours of soak time in L-AA (Figure 2.3.2: Fourier transform infrared spectrum for graphene oxide films comparing NUV-irradiated with unirradiated after one hour (A), two hours (B), three hours (C), and four hours (D) of exposure to l-ascorbic acid.C). After three hours of continuous NUV-radiation (Figure 2.3.2: Fourier transform infrared spectrum for graphene oxide films comparing NUV-irradiated with unirradiated after one hour (A), two hours (B), three hours (C), and four hours (D) of exposure to l-ascorbic acid.C), samples show a clear flattening of the peak corresponding to the C-OH bonds bending, which is an indication that reduction is taking place.

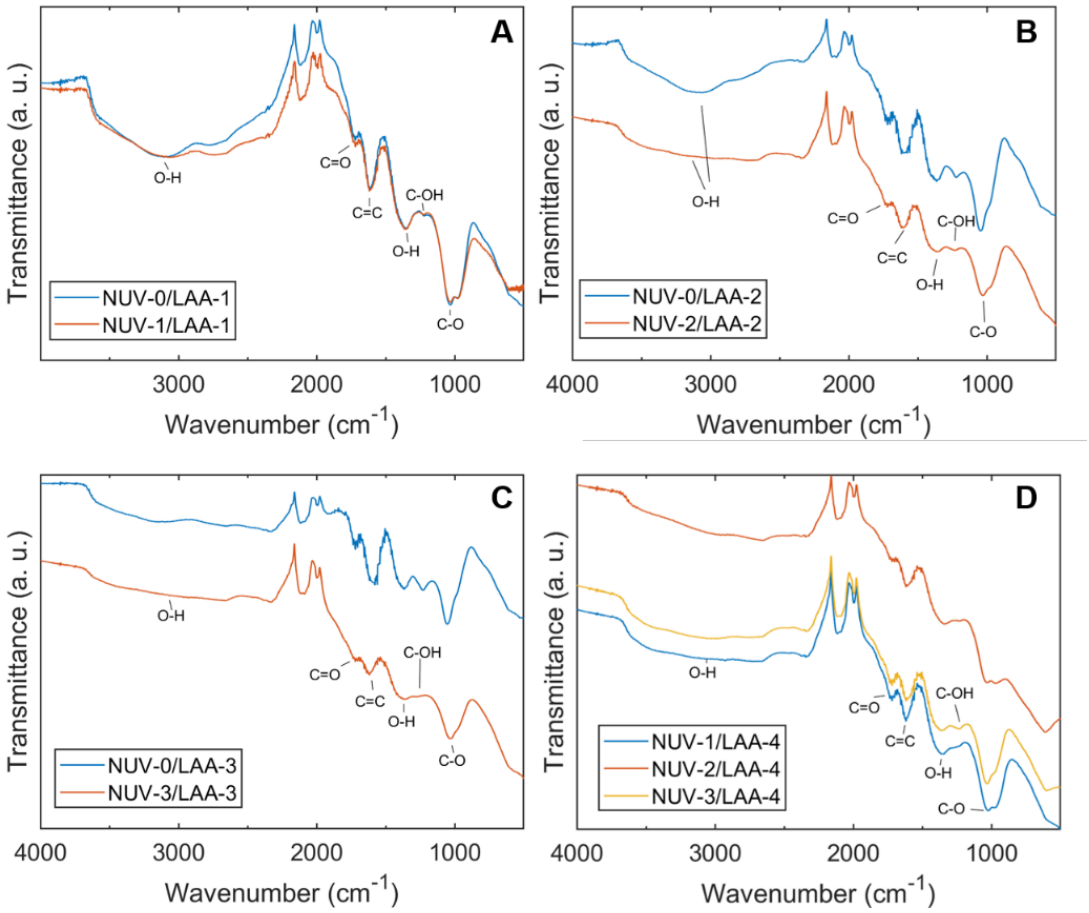

Figure 2.3.2: Fourier transform infrared spectrum for graphene oxide films comparing NUV-irradiated with unirradiated after one hour (A), two hours (B), three hours (C), and four hours (D) of exposure to l-ascorbic acid.

2.3.3 Wide-angle x-ray scattering

WAXS was used to quantify the changes in interlayer spacing caused by the removal of oxygen functionalities in the GO films. The peak shift within the first three hours of reduction was compared between NUV-irradiated and unirradiated films (Figure 2.3.3.1: Wide angle x-ray scattering spectra of pulverized graphene oxide films with increasing exposure to l-ascorbic acid alone (A) and NIV radiation (B). Additionally, WAXS spectra of GO films irradiated after 48 hours of exposure to L-AA solution compare (C) the two NUV radiation extremes (0 hours vs 3 hours) and (D) different NUV radiation times.). A noticeable shift occurred within the first hour

regardless of radiation conditions, decreasing the spacing of 8.07 Å by 0.91 Å and 0.76 Å from NUW-radiation with L-AA solution and L-AA solution alone respectively. This large shift is caused by the repacking of the GO layers from the initial removal of oxygen containing groups due to the exposure to L-AA. The peak at 2θ angle 26.5° (d = 3.36 Å), is observed in all samples and is due to residual graphite from the commercial GO solution[98].

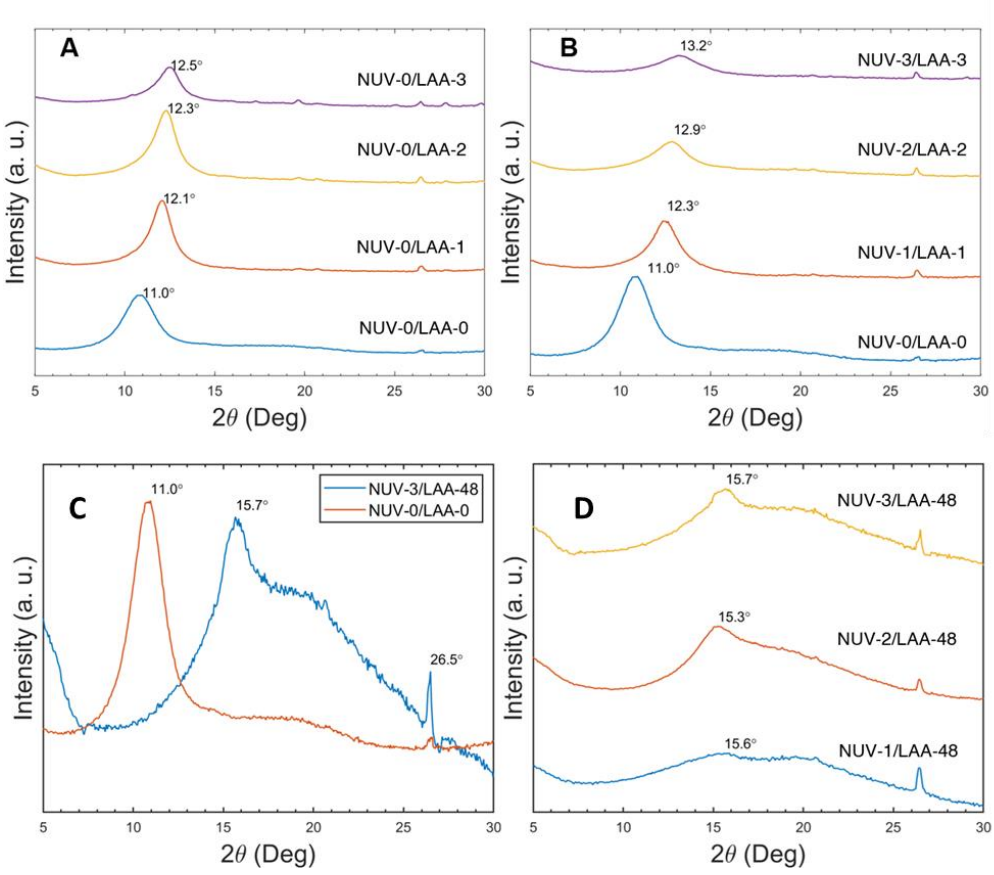

Figure 2.3.3.1: Wide angle x-ray scattering spectra of pulverized graphene oxide films with increasing exposure to l-ascorbic acid alone (A) and NIV radiation (B). Additionally, WAXS spectra of GO films irradiated after 48 hours of exposure to L-AA solution compare (C) the two NUV radiation extremes (0 hours vs 3 hours) and (D) different NUV radiation times.

After the first hour, differences in peak location, and therefore interlayer spacing, between NUV-irradiated and unirradiated samples became more prominent. While samples immersed in L-AA solution indicated a decrease in spacing by 0.14 Å between the second hour and 0.10 Å between the second and third hour, irradiated samples saw a more notable decrease in

spacing of 0.30 Å between the first and second hour and 0.10 Å between the second and third hour. This difference was attributed to NUW light assisting in further degrading the l-ascorbic acid ion, l-ascorbate, into dehydroascorbic acid at a faster rate (Figure 2.3.3.2: L-ascorbic acid degradation (sped up by NUV light) into l-dehydroascorbic acid yielding two H^+ ions which act as antioxidants and react with hydroxyls and epoxies in the surface of graphene oxide.), and issue well studied in produce containing high concentrations of vitamin C with beneficial effects in the reduction of GO[86,99]. It was also noted that the decrease in spacing does not occur at a linear rate as demonstrated by both conditions. A greater decrease in the rate is seen in NUV-irradiated samples potentially caused by the consumption of L-AA and decrease of oxygen containing groups.

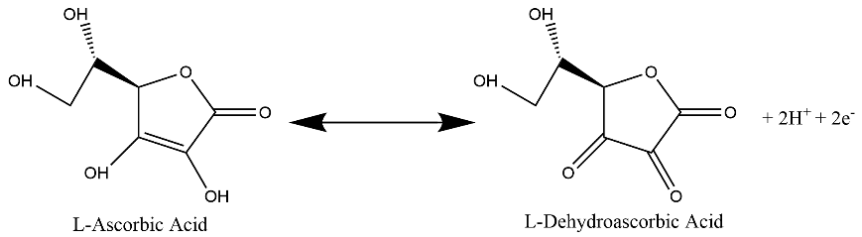

Figure 2.3.3.2: L-ascorbic acid degradation (sped up by NUV light) into l-dehydroascorbic acid yielding two H^+ ions which act as antioxidants and react with hydroxyls and epoxies in the surface of graphene oxide.

No significant reduction occurred past 25 hours in the segments of the GO film that were partially reduced. Films exposed to L-AA for longer periods, 24 hours to 48 hours, displayed relatively similar locations of peaks at 2θ angles near 15.6° (d = 5.68 Å) independent of radiation time as shown in Figure 2.3.3.1: Wide angle x-ray scattering spectra of pulverized graphene oxide films with increasing exposure to l-ascorbic acid alone (A) and NIV radiation (B). Additionally, WAXS spectra of GO films irradiated after 48 hours of exposure to L-AA solution compare (C) the two NUV radiation extremes (0 hours vs 3 hours) and (D) different NUV radiation times.. Moreover, a broad, intense peak appeared past the 20.0° (d = 4.44 Å), characteristic of partially reduced graphene oxide and near full reduction[100]. These peaks

confirm the reduction of graphene oxide is taking place to various degrees within the films, achieving results comparable to previous studies using hydrazine as a reductant[89]. In the previous study of hydrazine-reduced GO films, a bimodal distribution of unreduced and reduced GO film.

In this study, all of the starting material was involved in the reduction process. One fraction of the material gave rise to a break diffraction peak (2θ = 15.6°-26.5°), indication of reduced graphene oxide and its corresponding distorted, non-crystalline stacking of graphene sheets; the other fraction of the material exhibited partial reduction with L-AA intercalation, but incomplete removal of resulting species from the interlayers (Figure 2.3.3.1: Wide angle x-ray scattering spectra of pulverized graphene oxide films with increasing exposure to l-ascorbic acid alone (A) and NIV radiation (B). Additionally, WAXS spectra of GO films irradiated after 48 hours of exposure to L-AA solution compare (C) the two NUV radiation extremes (0 hours vs 3 hours) and (D) different NUV radiation times.A & B). The broadness is further evidence to suggest the uniformity of the reduction method.

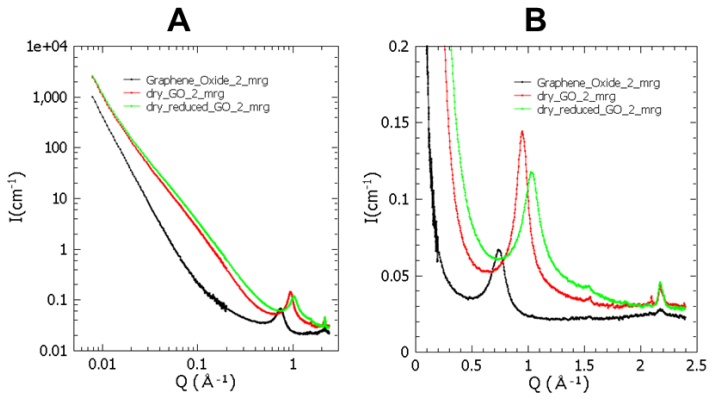

Figure 2.3.3.3: X-ray scattering of graphene oxide as received, and graphene oxide and reduced graphene oxide, each vacuum dried for 15 hours at 120 °C. A) SAXS region showing vacuum dried samples exhibited excess scattering which corresponds to correlation lengths of 24 Å for dry GO and 30 Å for dried reduced GO. B) WAXS data showing low-angle diffraction peaks. The non-dry GO sample has the lowest Q value peak corresponding to the largest interplanar d-spacing.

In conjunction to performing WAXS measurements on the GO films, small-angle x-ray scattering (SAXS) was performed (Figure 2.3.3.3: X-ray scattering of graphene oxide as

received, and graphene oxide and reduced graphene oxide, each vacuum dried for 15 hours at 120 °C. A) SAXS region showing vacuum dried samples exhibited excess scattering which corresponds to correlation lengths of 24 Å for dry GO and 30 Å for dried reduced GO. B) WAXS data showing low-angle diffraction peaks. The non-dry GO sample has the lowest Q value peak corresponding to the largest interplanar d-spacing.). SAXS revealed that only surface scattering could be seen from the non-dried graphene oxide. This was indicated by the featureless constant slope of about 3.5 in the log-log representation of the SAXS data. However, the dried materials have a significant additional scattering which deviated the most from the non-dried GO sample over a Q-range near Q=0.1 $Å^{-1}$. Additionally, WAXS (Figure 2.3.3.3: X-ray scattering of graphene oxide as received, and graphene oxide and reduced graphene oxide, each vacuum dried for 15 hours at 120 °C. A) SAXS region showing vacuum dried samples exhibited excess scattering which corresponds to correlation lengths of 24 Å for dry GO and 30 Å for dried reduced GO. B) WAXS data showing low-angle diffraction peaks. The non-dry GO sample has the lowest Q value peak corresponding to the largest interplanar d-spacing.) also revealed that drying had a big impact in the low angle peak position, changing the d-spacing from 8.46 Å (with atmospheric H_2O) to 6.62 Å dried under vacuum ay 120C for approximately 15 hours. Dry GO vs reduced GO showed a difference from 6.62 Å to 6.09 Å which led to the conclusion that drying conditions were reducing GO films as well, therefore a milder temperature (60C) was used to dry the films subsequently.

2.3.4 X-ray photoelectron spectroscopy

X-ray photoelectron spectroscopy (XPS) was used to track the decrease in concentrations of oxidized C species ($C\text{-}O_x$) as a function of exposure time to NUV-radiation and l-ascorbic acid (L-AA). Initial GO films showed an O/C ratio of 0.29 which is much lower than GO synthesized through the modified Hummer Method (0.41)[101]. The lower O/C ratio could be due to the presence of graphite contaminants in the commercial GO solution used. This is further

supported by the WAXS results through the presence of the graphitic peak at $2\theta = 26.5°$, present in all samples regardless of NUV radiation or L-AA exposure. The effects of continuous NUV exposure were studied by comparing the C1s spectra (Figure 2.3.4.1: Comparative C1s XPS spectra stackings for unirradiated (A) and NUV-irradiated (B) graphene oxide films for the first three hours, after 24 hours (C) and after 48 hours of treatment with l-ascorbic acid solution.) and C-C bond concentration (Figure 2.3.4.1: Comparative C1s XPS spectra stackings for unirradiated (A) and NUV-irradiated (B) graphene oxide films for the first three hours, after 24 hours (C) and after 48 hours of treatment with l-ascorbic acid solution.) of irradiated films with non-irradiated films for the first three hours. In all three instances, irradiated films show a larger degree of reduction in comparison to the un-irradiated films as observed by the increase in intensity of the peak near a binding energy of 285 eV (C-C) and the decrease of the peak near a binding energy of 287 eV (O-C=O). Additionally, while irradiated samples displayed some reductive behavior having an increase in C-C bond concentrations, the opposite was observed in un-irradiated samples. A large variance in reduction of the film was noted in the data acquired for unirradiated samples increasing with every hour.

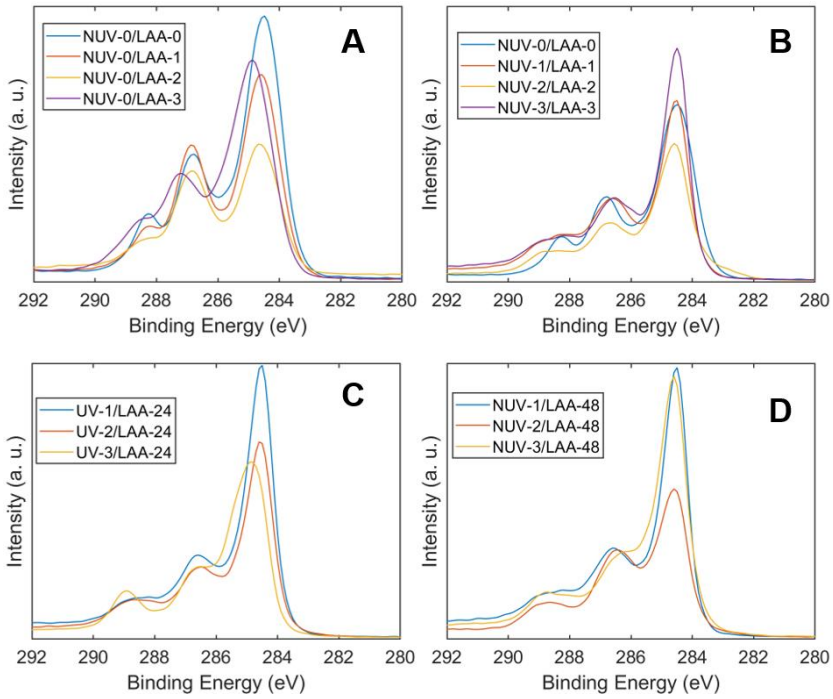

Figure 2.3.4.1: Comparative C1s XPS spectra stackings for unirradiated (A) and NUV-irradiated (B) graphene oxide films for the first three hours, after 24 hours (C) and after 48 hours of treatment with l-ascorbic acid solution.

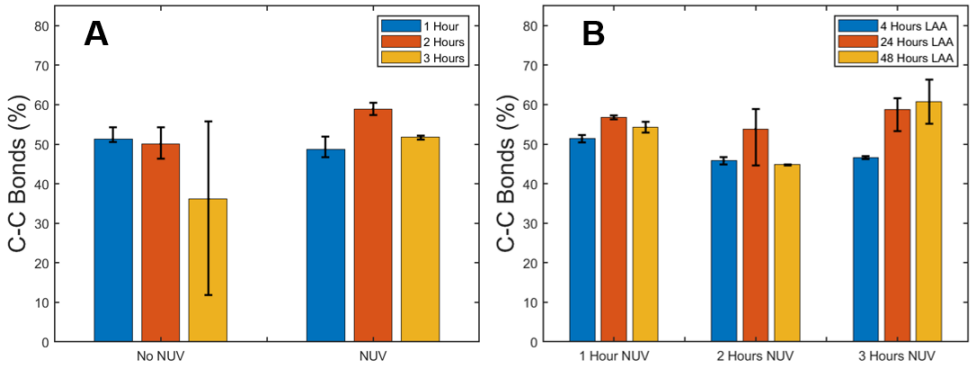

Figure 2.3.4.2: Comparison of C-C bond concentration in NUV irradiated with unirradiated samples in the first three hours (A) and different LAA solution exposure times (B).

2.3.5 Discussion

The variation in the reduction of the graphene oxide films could be largely due to the intercalation of water and L-AA reduction byproducts in the GO stackings, a common problem with green reductants as illustrated in Figure 2.3.5.1: Schematic of GO films demonstrating the

effect that vacuum drying has on the casted films before and after reduction based on WAXS and XPS results.[100]. When drop-casted, the graphene oxide sheets tend self-align and stack neatly on top of one another forming a film with roughly one water molecule hydrogen bonded between the oxygen functional groups of two GO layers, as evident from the presence of the OH band in the FT-IR results. Upon vacuum drying, the film begins to repack as moisture between the stacks dissipates[102]. Due to the hydrophilic nature of GO, pockets with water molecules can form, as demonstrated by the WAXS results (Figure 2.3.3.3: X-ray scattering of graphene oxide as received, and graphene oxide and reduced graphene oxide, each vacuum dried for 15 hours at 120 °C. A) SAXS region showing vacuum dried samples exhibited excess scattering which corresponds to correlation lengths of 24 Å for dry GO and 30 Å for dried reduced GO. B) WAXS data showing low-angle diffraction peaks. The non-dry GO sample has the lowest Q value peak corresponding to the largest interplanar d-spacing.). When immerse in L-AA solution, reduction begins on the surface of the film and slowly makes its way through paths created from spaces and cavities in the loosely stacked structures[102] entering tight areas of the inner layers of the film. Vacuum drying releases the moisture in the films but may leave adsorbed molecular water and L-AA residuals (gluronic and oxalic acids) which may from hydrogen bonds with residual oxygen functionalities[86] that could not be removed easily through washing.

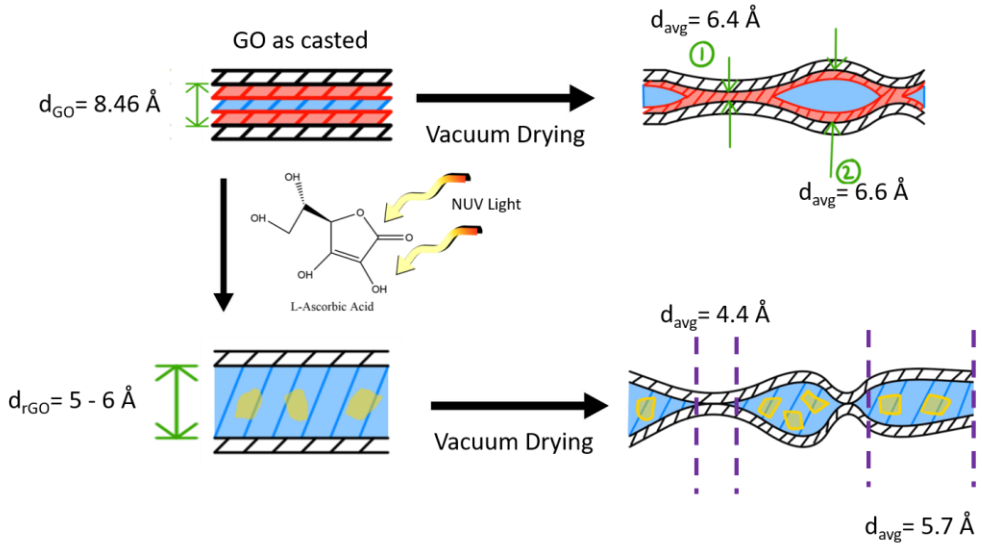

Figure 2.3.5.1: Schematic of GO films demonstrating the effect that vacuum drying has on the casted films before and after reduction based on WAXS and XPS results.

It is shown in literature that graphene oxide paper/films can rapidly desorb around 80% of the adsorbed moisture using wrinkle-like tunnels such as those shown in Figure 2.3.1: Scanning electron micrographs of graphene oxide films treated with l-ascorbic acid and near ultraviolet light displaying folds on the surface (A and B). Cross-sectional micrographs of the film reveal waviness in a stacked structure.[97]; however, other factors affect the moisture desorption of the reduced graphene oxide film. As Boukhalov et al. have demonstrated through simulation, the interlayer distance between graphene sheets plays a crucial role in the water permeation mechanism[103]. The decrease in interlayer distance from the reduction of the graphene oxide can make the membrane 100 times les permeable to water and create blockage when the interlayer spacing drops to around 4 Å, as demonstrated experimentally by Nair et al [104]. While it is suggested that the formation of percolated capillaries from unoxidized or reduced regions assist the flow of water[103], the probability of lenticular pores forming between impermeable passages which would essentially seal the water in cannot be discarded. Due to the modest heat applied during the vacuum drying to limit influence on reduction, it is unlikely that

lenticular pores would be ruptured. In addition, intercalated water in the films can restrict the movement of other molecules. In this case gluronic and oxalic acids whose presence near the film's surface can influence the XPS readings. Du to the impermeability to molecules other than water, chemical approaches are not suggested as appropriate methods to reduce graphene oxide stacked structures such as films, membranes, or papers.

Most samples that have been irradiated demonstrate significantly less variance in the degree of reduction. This could be due to the NUV light penetrating past the surface layers. Since graphene oxide has relatively lower absorbance at the visible NUV light range (400-405 nm) than UW light. This means that NUV light can reach deeper into the film and partially reduce the graphene oxide in the center layers of the film up to a certain depth[105]. Go et al. [106] have shown through UV-Vis that UV light is capable of reducing graphene oxide at a similar rate as L-AA alone; however, these experiments were done using 252 nm UV-radiation which can lead to some discrepancies since GO has a greater absorption at that particular wavelength.

The concentrations of C-C bonds in the samples were measured after being exposed to L-AA for four hours, 24 hours, and 48 hours at the three NUV-radiation levels (Figure 2.3.4.1: Comparative C1s XPS spectra stackings for unirradiated (A) and NUV-irradiated (B) graphene oxide films for the first three hours, after 24 hours (C) and after 48 hours of treatment with l-ascorbic acid solution.) and the statistical significance of these results was validated using Minitab. The normal probability plots indicate that the results follow a normal distribution and are statistically acceptable for design of experiment analysis. From the main effect plot, it was determined that all factors are significant with exposure to L-AA having the highest impact, followed by the interaction between L-AA and NUV exposure, and lastly NUV-radiation meaning that after the initial NUV-exposure, the reduction of the film became more dependent

on the exposure to L-AA. While NUV light works in conjunction with L-AA to reduce the surface of the film, L-AA plays a more important role after the radiation in reducing the underlying layers, therefore, exposure to L-AA is necessary to reduce inner layers of the film and improve uniformity. The low impact of NUV exposure alone is likely cause by the reduction of the film's surface. As the film was irradiated and reduced, graphene oxide began absorbing more light at 405 nm wavelength[106] until reaching a point where the effects of NUV light were negligible. After this point only the solution that has entered the inner layers of the film through gaps furthered the reduction.

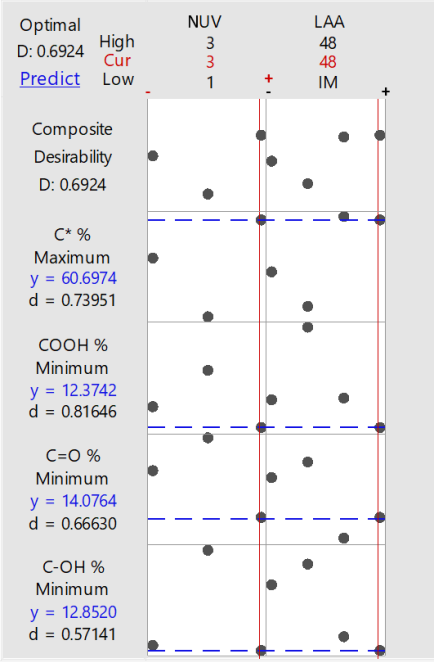

Figure 2.3.5.2: Optimization plot with the individual evaluated factors (columns) and their effect on the responses (rows) based on the bond percentages observed from XPS results.

The optimization graph obtained through design of experiment (Figure 2.3.5.2: Optimization plot with the individual evaluated factors (columns) and their effect on the responses (rows) based on the bond percentages observed from XPS results.) suggests that the combination that will maximize the reduction are longer NUV-exposure time (three hours) and

longer exposure to L-AA (48 hours) producing samples with a C-C bond concentration of 60.70% and an O/C ratio of 0.23, which is comparable to, although higher than, GO suspensions reduced by green reductants ().

Table 2.3.5: Comparison of O/C ratio in most reduced samples reported (three-hour NUV-radiation and 48 hours of L-AA exposure) with values reported in literature from other green reductants.

Green Reduction Method	O/C Ratio	Source
This report:	0.23	[107]
Ginseng	0.20	[76]
Natural Cellulose	0.18	[77]
Baker's Yeast	0.17	[78]
Hydrogen Rich Water	0.21	[75]
Gallic Acid	0.19	[79]
Pulsed Laser	0.21	[83]
Urea	0.18	[80]
L-Ascorbic Acid (Aqueous Dispersion)	0.17	[86]

2.4 CONCLUSION

The effect of NUV light in conjunction with l-ascorbic acid (L-AA) on the reduction of graphene oxide films was characterized using SEM, FT-IR, WAXS, and XPS. It was determined that NUV-radiation at 405 nm wavelength can promote the reduction of graphene oxide by not only accelerating the degradation of L-AA and subsequently the reduction of graphene oxide, but also increasing the depth of reduction from the surface layers to the layers in between the film. Samples exposed to 3 hours of NUV-radiation also showed that longer exposures of NUW-radiation can have a significant impact in the reduction of graphene oxide films within the first

hours, meaning that longer exposure is recommended to obtain a more uniformly reduced film. Exposure time in L-AA was also proven to be a main factor in reducing the graphene oxide past the surface layer, with 48 hours of exposure showing concentrations of C-C bonds up to 60.7% and the presence of an intense peak in the 2θ angle near 20.0°, comparable to solution processed graphene oxide reduced by other green methods. However, it is important to note that the lowered permeability of the reduced film may entrap moisture and chemical residuals from the reductant. Still, alternately to using high temperature thermal annealing which can result in blistering of the film due to the volatile release of vapors and air or other chemical methods with a large variance in reduction of the film, the use of L-AA synergistically with NUV-radiation can produce stable GO films with tailored reduction.

Chapter 3: Synthesis for water-induced stiffening epoxy vitrimer

3.1 Introduction

Polymers can be categorized into thermoplastics of thermosets depending on the type of bonding that holds the polymer network together, each with their own advantages and disadvantages depending on the application[32]. While thermoplastic polymers tend to be weaker, the physical bonds that form them allow for reprocessing and recyclability. On the other hand, thermoset polymers cannot be reprocessed once fully cured, but due to their strong covalent bonds, these materials are typically stronger, more chemically resilient, and thermally stable. Thermoset polymers, however, can achieve the plasticity of thermoplastics through the introduction of exchangeable chemical bonds in the covalent crosslinks forming dynamic crosslinks. This exchange mechanism allows the material to flow while not permanently altering the material's properties. Polymers with these types of exchangeable bonds are known as covalent adaptive networks (CANs)[108]. Polymers containing CANs can respond to an applied stimulus such as heat or pressure and are capable of reconfiguring their network topology or reforming broken bonds through intricate chemical processes[33].

Vitrimers are associative CANs that show a gradual viscosity decrease after heating due to the transesterification reaction in epoxy/acid networks[109]. These novel materials display a shift in crosslink position upon the application of heat but retain the same number of crosslinks, exhibiting a fixed crosslink density in the network. This fixed crosslinked density avoids dissolvement in the material. One of the chemistries that can form vitrimers is disulfide exchange which undergo a radical mediated mechanism[110]. 4-aminophenyl disulfide is a hardener used for the design of reprocessable and recyclable epoxy vitrimer[111]. This exchange mechanism

occurs faster and at lower temperatures than other types of reactions such as Diels-Alder[112], imine bonds[113], and coordination bonds[114].

Due to their CANs, some vitrimers have shown other functional properties. In the case of 4-aminophenyl disulfide, cleaving the S-S bonds produces a bright green discoloration[111]. For the first vitrimer project, we explored ceramic filler to enhance the mechanochromic effect of the disulfide vitrimer. The aminophenyl disulfide isomer, 2-aminophenyl disulfide, has shown potential for self-healing applications[115]. The second and third vitrimer projects aim to adapt the disulfide vitrimer with 2-aminophenyl disulfide for additive manufacturing and facile templating.

3.2 SYNTHESIS OF SELF-SENSING POLYMER COMPOSITES

3.2.1 Materials, synthesis and fabrication

Bisphenol A diglycidyl ether (BADGE) (340.41 g/mol) and 4-aminophenyl disulfide (4AFD) (248.37 g/mol) were purchased from Sigma Aldrich (Darmstadt, Germany). Barium titanate powder (200 nm average particle size) was purchase from Inframat Advanced Materials (Connecticut, United States), alumina powder (0.1 μm average particle size) and silica powder (11 nm average particle size) were purchased from Sigma Aldrich (Darmstadt, Germany). Glass hollow spheres (HGS) were kindly provided by the Kansas City National Security Campus. Vitrimer composites were synthesized by first melting the BADGE resin at 85 °C. Once fully melted, the dynamic hardener 4AFD was added to the resin and mixed with a magnetic stirrer for 15 minutes at 85 °C. Afterwards, different weight percentages (Table 3.2.1: Vitrimer compositions tested for mechanochromism.) of ceramic powders were added to the epoxy resin and were allowed to mix for 10 minutes at the same temperature. The resin was then poured into silicone molds and cured for 5 hours at 150 °C.

Table 3.2.1: Vitrimer compositions tested for mechanochromism.

Sample	Ceramic Filler	Wt %
Vit-HGS-1	Hollow Glass Spheres	0.1
Vit-HGS-2	Hollow Glass Spheres	1.0
Vit-SiO2-1	SiO_2	0.1
Vit-SiO2-2	SiO_2	1.0
Vit-BaTiO3-1	$BaTiO_3$	1.0
Vit-BaTiO3-2	$BaTiO_3$	50.0
Vit-Al2O3-1	Al_2O_3	1.0
Vit-Al2O3-2	Al_2O_3	50.0

3.2.2 Material characterization

The mechanochromic effect of pure vitrimer and vitrimer composites was evaluated from the color change after the application of mechanical force. First, samples were subjected to abrasive forces using sandpaper of grit size 240. Scratch testing was done by gently scratching the surface of the vitrimer composites with a stainless-steel needle. Response to impact was tested impacting the sample with hammer with a small spherical end.

3.2.3 Results and discussion

When pure vitrimer samples were subjected to abrasive forces using sandpaper and through scratching with stainless-steel needle, the samples produced a bright discoloration in the afflicted surfaces as well as in the dust produced from sanding (Figure 3.2.3.1: 4AFD vitrimer after being subjected to abrasive forces.). Pure vitrimer samples, however, were unresponsive when impacted with a hammer.

Figure 3.2.3.1: 4AFD vitrimer after being subjected to abrasive forces.

Vitrimer-HGS composites showed similar response to abrasive forces such as sanding and scratching as pure vitrimer. With a greater color contrast between the discoloration and the vitrimer composite, the mechanochromic effect was more easily distinguished. When impacted with a hammer, vitrimer-HGS composites produced same discoloration as in the impacted surfaces. The mechanochromic effect, although not as vivid as in the impacted surfaces, could also be observed in surfaces of the cracks, a result of the impact testing. Vitrimer-SiO2, vitrimer-BaTiO3, and vitrimer-Al2O3 composites only responded to scratching which produced a dark discoloration as opposed to the pure vitrimer and vitrimer-HGS composites. These vitrimer-ceramic composites also did not respond to any other mechanical forces tested, even at higher weight percentages despite the color contrast. At 50 wt% of Al_2O_3 filler, the vitrimer- Al_2O_3 showed increased response but only in the surfaces surrounding burst air bubbles.

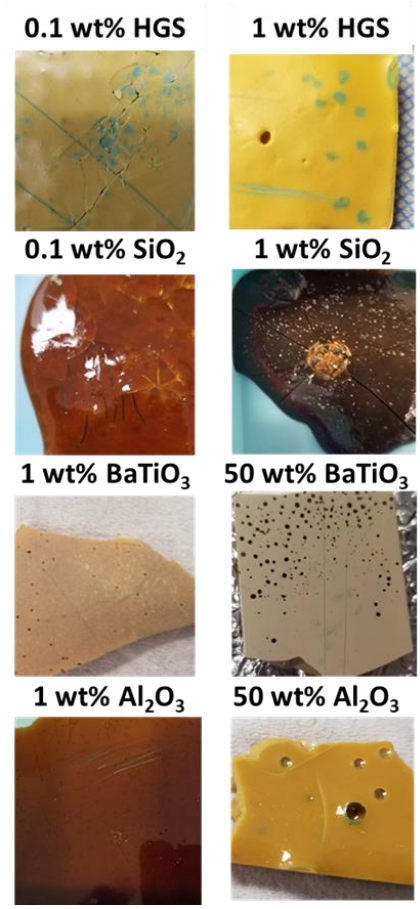

Figure 3.2.3.2: Multiple vitrimer composites formed with HGS, SiO_3, $BaTiO_3$, and Al_2O_3 with varying concentrations of ceramic filler.

3.3 VITRIMER PRINTING

3.3.1 Materials and synthesis

Bisphenol A diglycidyl ether (BADGE) (340.41 g/mol), 2-aminophenyl disulfide(2AFD) (248.37 g/mol), and polyethylene glycol 1500 (PEG1500) were purchased from Sigma Aldrich (Darmstadt, Germany). Graphene oxide in a 5 mg/mL suspension was purchased from Goographene (Virginia, United States). Pure vitrimer samples were synthesized by first melting the BADGE resin at 85 °C and mixing 2AFD at the same temperature for 15 minutes. Vitrimer composites were synthesized by first melting the BADGE resin at 85 °C. Once fully melted, 0.8 mL of graphene oxide solution was added to the melted BADGE and mixed at 100 °C to evaporate the water from the graphene oxide suspension. Afterwards the dynamic hardener,

2AFD, was added to the resin and mixed with a magnetic stirrer for 15 minutes at 85 °C. Afterwards, 5 wt% of PEG1500 was added to the epoxy resin and were allowed to mix for 10 minutes at the same temperature. The resin was then poured into silicone molds and cured for 1.5 hours at 150 °C.

3.3.2 Fabrication

A Hyrel Engine HR equipped with a KR-15 direct write heated extruder was used to print. Pure vitrimer was extruded at 80 °C while vitrimer-GO-PEG composites were extruded at 90 °C. Test geometries such as a 10x10x10 mm^3 cube and a dinosaur were printed to validate the material's capability to extrude and print. Further testing was done to attempt to obtain mechanical testing samples in accordance to ASTM standard D638.

3.3.3 Results and Discussion

Initial success was achieved printing small geometries with the pure vitrimer formulations (Figure 3.3.3.1: Successful first prints of small and complex geometries through FFF.). The pure vitrimer formulation was extruded with a 0.8 mm nozzle at 80 °C which allowed for the printing of complex structures such as overhangs without the need of supports structures. This is due to how close the vitrimer was to the solidification temperature which meant the vitrimer could cool and harden very rapidly. The highest achievable resolution with the pure vitrimer formulation was of 0.2 mm at 90 °C, however, unlike the 0.8 mm nozzle, it was unable to print overhangs from the need to cool longer to harden. The same vitrimer used to print the structures in Figure 3.3.3.1: Successful first prints of small and complex geometries through FFF. was reused for two months of continuous recycling with no significant deterioration. Towards the end of the vitrimer's recyclable life, the vitrimer became rubbery. Printing at the higher temperatures required for smaller diameter nozzles significantly reduced the vitrimer's

recyclable life with every print since each time the vitrimer was extruded, it required a higher temperature to print.

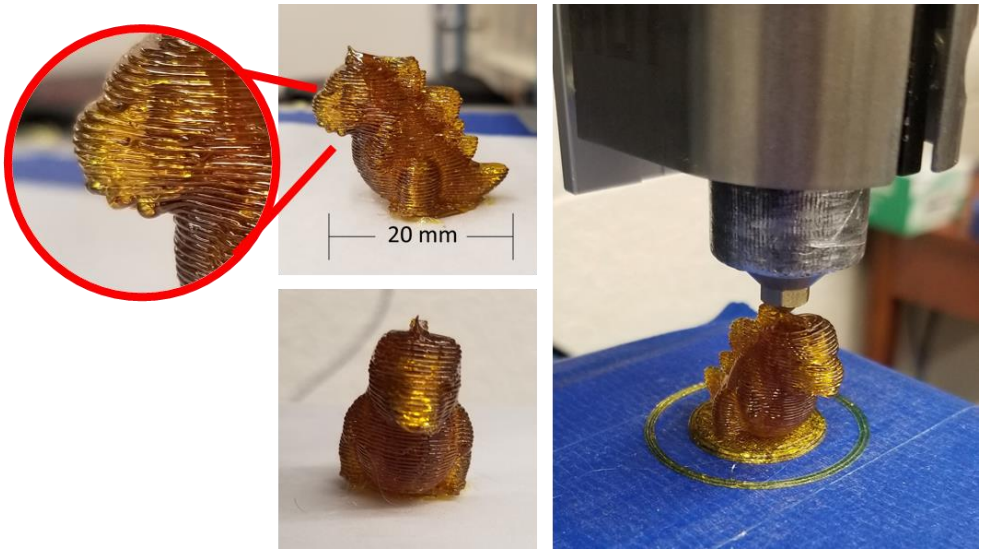

Figure 3.3.3.1: Successful first prints of small and complex geometries through FFF.

When printing larger geometries such as ASTM Standard D638 Type V dog bone samples, printed parts suffered from brittle properties. Attempting to remove the parts from build platform resulted in cracking and failure, making the removal process difficult. To address the issue of low part strength and limited recyclability at higher resolutions, graphene oxide (GO) and polyethylene glycol 1500 (PEG1500) were added to the formulation. GO filler added increased the toughness of the epoxy vitrimer and allowed for extrusion at lower temperatures as Krishnakumar et al have demonstrated[115]. This facilitated the removal and printing process; however, GO also decreased the recyclable life of the vitrimer, making the stock material reach a rubbery state sooner. PEG1500 was added to as a retardant and a plasticizer at the printing temperature. The free volume added by the inert chains of PEG1500 facilitates the recombination of dynamic covalent bonding and limits the formation of new crosslinks which would restrict the

flow of the vitrimer[116]. This, in term, lengthens the recyclable life of the vitrimer. Further studies are needed to further validate the pot-life and recyclability of the enhanced vitrimer resin.

3.4 WATER-INDUCED STIFFENING VITRIMER

3.4.1 Experimental details

3.4.1.1 Materials, synthesis, and fabrication

Bisphenol A diglycidyl ether (BADGE) (340.41 g/mol), 2-aminophenyl disulfide(2AFD) (248.37 g/mol), and polyethylene glycol 400 (PEG400) were purchased from Sigma Aldrich (Darmstadt, Germany). Vitrimer composites were synthesized by first melting the BADGE resin at 85 °C. Once fully melted, the dynamic hardener 2AFD was added to the resin and mixed with a magnetic stirrer for 15 minutes at 85 °C. Afterwards, 50 wt% of PEG400 was added to the epoxy resin and were allowed to mix for 10 minutes at the same temperature. The resin was then poured into silicone molds and cured for 20 hours at 150 °C. Water-treated vitrimer composites were soaked in water at room temperature for 24 hours and then left to dry in air overnight. Water-treated samples were then placed in an oven at 80 °C for 10 minutes after air drying to allow the vitrimer composite to relax and undo any curling that may result during the drying process.

3.4.1.2 Material characterization

The surface morphology of the vitrimer composites and phase separation on the cross-sectional area were analyzed using a Thermo Scientific (Massachusetts, United States) Phenom ProX scanning electron microscope at 15 kV accelerating voltage and with a backscatter electron detector. The change in molecular structure of the vitrimer composites after water and heat treatment was analyzed through Fourier transform infrared (FT-IR) spectroscopy using a Thermo Scientific (Massachusetts, United States) Nicolet iS5 Infrared Spectrometer. X-ray diffraction

measurements to analyze changes in the composite's crystallinity at the surface and polished cross-sectional area were carried out using a Brucker (Massachusetts, United States). Tensile mechanical testing of the vitrimer composites was done in accordance with ASTM Standard D638 at a strain rate of 1 mm/minute using an Instron (Massachusetts, United States) 5886 mechanical load frame with a video extensometer.

3.4.2 Results and discussion

3.4.2.1 Microscopy

The phase separation effect was visible through optical microscopy in thin samples (~2 mm thickness). As casted samples did not show any unique features and looked homogenous throughout. When wetted, the vitrimer composites formed spherical features, attributed to to the phase separation induced by the water absorption. After removing the vitrimer composite and allowing it to dry in air for 24 hours, the features on the vitrimer remained more losely packed than when wet. The presence of these spherical features after wetting and even after drying, shows that they are composed of the PEG400 and not water. The microscope images are visual evidence to support that there is a phase separation occuring between the hydrophobic vitrimer and the hydrophilic PEG.

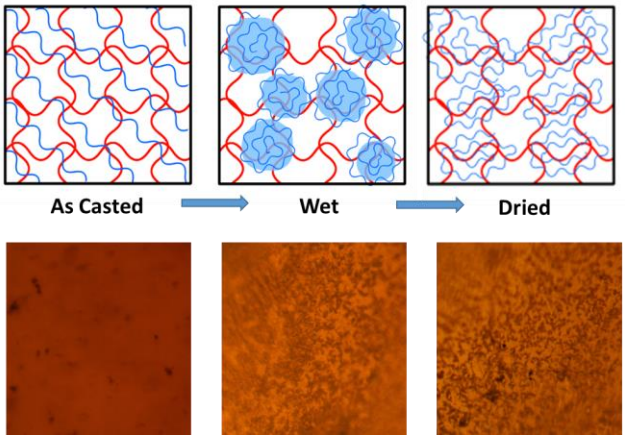

Figure 3.4.2.1: Schematic with microscope images of water induced phase separation in the vitrimer composite after exposure to water.

3.4.2.2 Mechanical properties

The stress-strain relationship of vitrimer composites was measured through tensile mechanical testing at room temperature using the strain ramp mode. The stress-strain behavior for dry vitrimer composites containing PEG400 was plotted in Figure 3.4.2.2: Mechanical results from (left) as casted PEG-vitrimer composites and (right) a comparison of as casted samples with samples processed with water and heat treated afterwards.. As observed, the modulus of elasticity is directly influenced by the amount of plasticizer present in the composite with more plasticizer leading to softer vitrimer composites. Figure 3.4.2.2: Mechanical results from (left) as casted PEG-vitrimer composites and (right) a comparison of as casted samples with samples processed with water and heat treated afterwards. also shows a comparison of the stress-strain behavior of the as casted samples with the samples post water/heat treatment. Vitrimer composites saw an improvement in mechanical properties post water/heat treatment leading to not only a 585x increase in elastic modulus but also 1.8x increase in strain at break and a 118x increase in ultimate tensile strength.

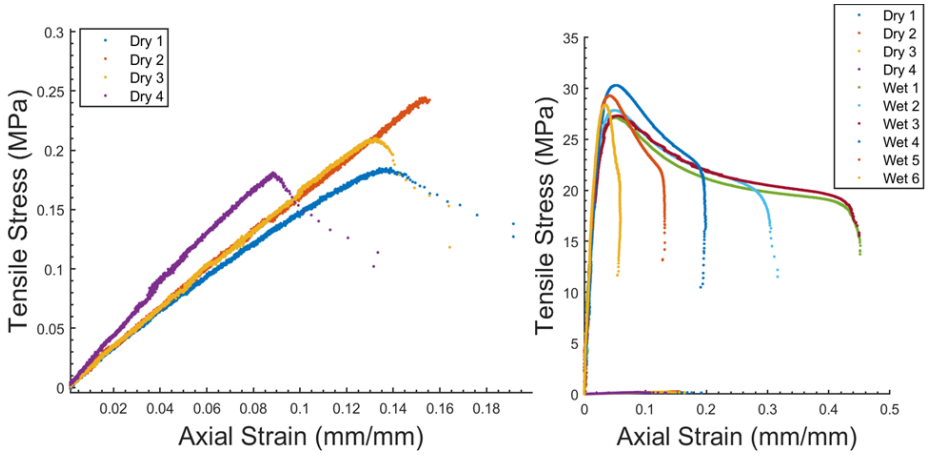

Figure 3.4.2.2: Mechanical results from (left) as casted PEG-vitrimer composites and (right) a comparison of as casted samples with samples processed with water and heat treated afterwards.

3.4.2.3 X-ray diffraction

X-ray diffraction was used to analyze changes in the crystallinity of the vitrimer composite at the surface. In all three stages of processing, as casted, after wetting, and after drying and post-heating, the vitrimer composites showed a high intensity in the broad peak in 2θ ranging from 10 °- 30 °, apparent in homogenously amorphous epoxy composites[117] which infers the that the polyethylene glycol is completely dispersed in the epoxy vitrimer. As casted vitrimer composites showed small diffraction peaks at 2θ values of 29.6 ° and 31.0 °. When the composites are wetted, these peaks are lost and replaced with a peak at 2θ = 26.7 °. In addition, the intensity of the amorphous peak decreased showing loss of amorphous structure due to the phase separation between the hydrophobic epoxy matrix and the hydrophilic plasticizer. After drying and post-heat treatment, the vitrimer composite show complete loss of crystalline structure.

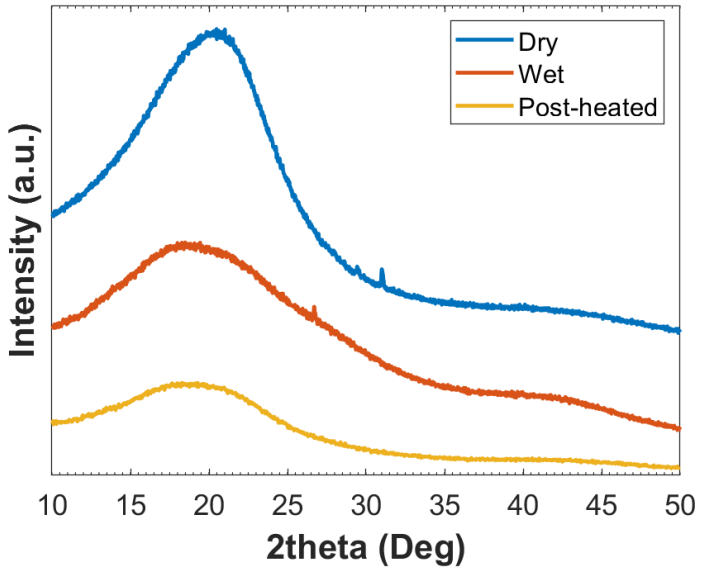

Figure 3.4.2.3: X-ray diffraction of PEG-vitrimer composites after casting, being exposed to moisture, and reheating after drying.

3.4.2.4 Fourier transform infrared spectroscopy

Fourier transform infrared spectroscopy (FT-IR) was used to analyze the changes in molecular structure of vitrimer blends. First, the absence of oxirane rings (914 cm^{-1}) indicates that the vitrimer composite is fully cured. The as casted vitrimer composite shows a chemical structure similar to bisphenol A ethoxylate, which has structure resembling bisphenol A diglycidyl ether with extended chains akin to polyethylene glycol chains. This demonstrates the compactness of the PEG400 plasticizer in the epoxy vitrimer crosslinks. After water treatment, the vitrimer composites lost their PEG structure at the 3000-2800 cm-1 range, showing a more similar structure to epoxy mixture. After heat treatment, the peak at 1670 cm-1 disappeared while a sharp peak at 1720 cm-1 appeared potentially from an oxidative reaction due to the presence of intercalated water.

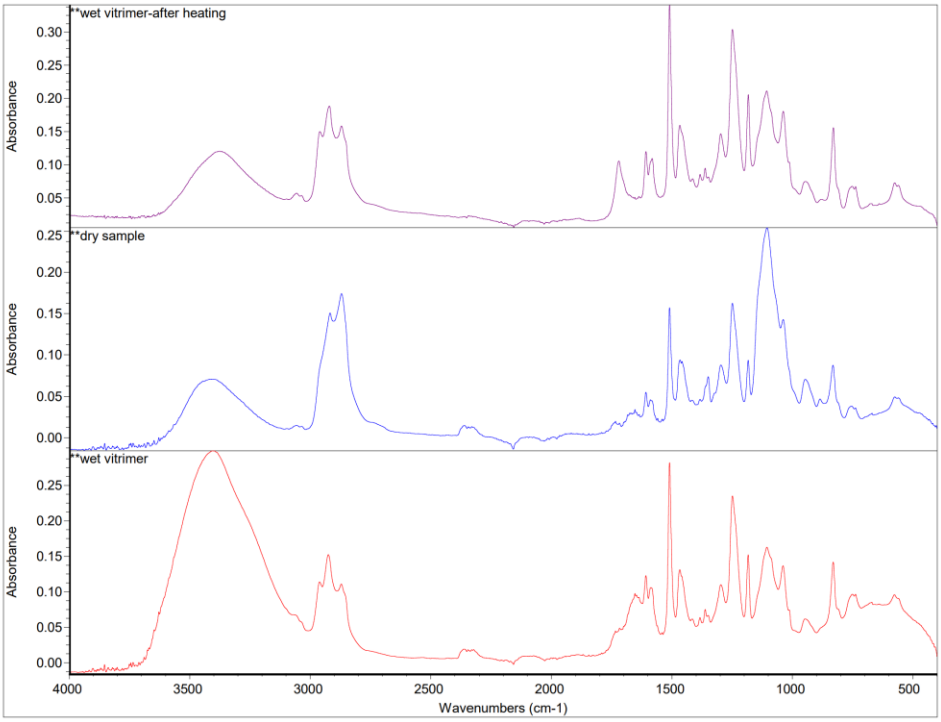

Figure 3.4.2.4: Fourier transform infrared spectroscopy showing the difference in molecular structure of PEG-vitrimer as casted, after wetting, and after drying and heat treatment.

3.4.2.5 Other observations

Other qualitative observations were made for the response of the vitrimer-PEG composites to water. Firstly, vitrimer composites that are not fully crosslinked show two types of hydrochromic response. When a casted vitrimer is exposed to water, the vitrimer changes from an amber color to a bright white. This is due to the disruption of the vitrimer network caused by the phase separation between the hydrophilic PEG chains and the hydrophobic epoxy chains[118]. The original amber color is restored over time upon drying or can be induced immediately at temperatures above 100 °C. When extruded from a nozzle, the vitrimer changes from a dark amber color to a very bright green, reminiscent of the mechanochromic vitrimer produced with the disulfide isomer 4-aminophenyl disulfide. The difference in color is likely due to the alignment of the semicrystalline domain causing the vitrimer to cleave at the disulfide bonds upon phases separation[119].

Figure 3.4.2.5.1: Discoloration of extruded (A, B) and casted (C) PEG-vitrimer composites.

The vitrimer-PEG composite's response to ethanol, another solvent for PEG, was also observed. In contrast to the composite's response to water, vitrimer-PEG composites partially dissolved when soaked in ethanol. Since PEG and uncured resin have a high solubility to ethanol rather than causing a phase separation, ethanol likely cause the PEG and vitrimer to become more miscible. This is highly probable since the PEG chains restrict the crosslinking of the

epoxy vitrimer and is more likely to retain the solubility of epoxy resin. The solubility test is also evidence to support that the phase separation is repentant on the difference in hydrophilicity between the two polymers.

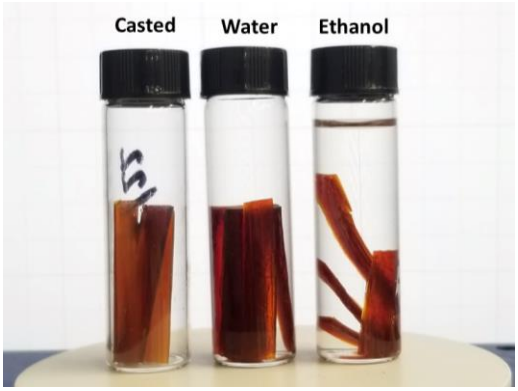

Figure 3.4.2.5.2: Solubility testing of PEG-vitrimer composite in water and ethanol.

Densification effects can also be observed on the vitrimer-PEG composites after water and heat treatment. The vitrimer composites swell upon exposure to water; however, upon drying see a reduction in volume (11%) with no significant mass loss. After heat treatment, the vitrimer composites form a transparent outer layer and an opaque center in the perfect shape of the casted composite's geometry.

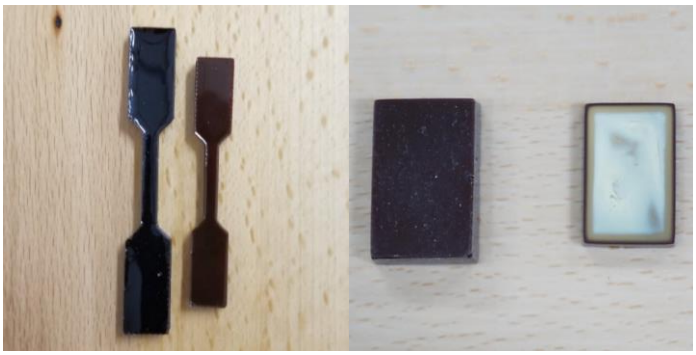

Figure 3.4.2.5.3: Changes in volume (A) and color (B) of PEG-vitrimer composited before (left) and after (right) exposure water and air drying.

3.5 CONCLUSION

Overall, properties of dynamic epoxies can be altered through filler material to obtain unique properties that fit a wide range of applications as demonstrated from the three vitrimer projects presented. From the synthesis of self-sensing polymer composites, it was demonstrated that mechanochromic vitrimer, synthesized with the dynamic hardener 4-aminophenyl disulfide, show greater response to mechanical damage with hollow glass sphere filler than pure vitrimer. The mechanochromic response from the vitrimer composites with other ceramic filler such as SiO_2, $BaTiO_3$, and Al_2O_3 do not better the sensing capabilities of the vitrimer despite having a greater color contrast to the expect color change. This shows that epoxy vitrimer has a high affinity with glass and the use of hollo particle filler can enhance the mechanochromic response.

From the printing of vitrimer synthesized with 2-aminophenyl disulfide, it was learned that the self-healing vitrimer had great potential for extrusion based additive manufacturing. Great success was demonstrated when printing small simple and complex geometries. The material's brittleness when printing larger structures was addressed through the incorporation of graphene oxide nanofiller for enhanced toughness and processability as well as polyethylene glycol for prolonging the recyclable life of the vitrimer. This opens the possibility for the use of additive manufacturing to process novel materials with functional properties.

Lastly, the water-induced effects of self-healing vitrimer-polyethylene glycol composites were studied. According to the analysis performed through x-ray diffraction, the change in crystallinity at the vitrimer surface shows that exposure to water removes polyethylene glycol from te surface. Fourier-transform infrared (FT-IR) spectroscopy and optical microscopy were both evidence to support the fact that phase separation was occurring between hydrophobic vitrimer and hydrophilic polyethylene glycol throughout the composites upon exposure to water.

Furthermore, the FT-IR analysis and mechanical response, and other visual observations such as color change in the center of the samples, suggest a strengthening reaction is occurring due to the PEG in the composite. These results demonstrate the ability to incorporate polyethylene glycol for ease of manufacturing through templating and the potential for the material to be used in structural applications due to the strength and toughness.

Chapter 4: Machine vision and machine learning for property prediction of syntactic foams and lattice structures

4.1 Introduction

The lack of qualification and property prediction of 3D printed parts is a challenge in AM which is being addressed through the use of machine learning. Machine learning is a series of procedures and algorithms that analyze data to recognize patterns, clusters, or trends for the extraction of useful information[39]. In AM, process parameters are obtained through loops of trial-and-error, a repetitive process which is largely dependent on the capabilities of an operator to recognize anomalies and make the corresponding adjustment[40]. However, these patterns can often be difficult to notice for which machine learning can easily draw inferences. Machine learning has been applied at various steps of the additive manufacturing process being used for design optimization prior to printing[41,42], quality assurance and defect detection in conjunction with machine vision during the printing process[43,44], and for performance prediction of the printed part after the process[45].

The first machine vision project aims to recreate the machine vision algorithm and machine learning result obtained by Roach et al., in which the properties of 3D printed foam replacement structures were predicted through visual analysis of the filament diameter, filament spacing, and number of layers[120]. The second machine vision project aims to form a more robust analysis of the microstructure in syntactic foams, which are composite materials in which porous particles are embedded in the matrix material[121]. Through the use of an image segmentation method known as STARDIST[122], we trained a model to be used for automated characterization and information gathering for machine learning.

4.2 MACHINE VISION/LEARNING FOR PROPERTY PREDICTION OF FOAM REPLACEMENT STRUCTURES

4.2.1 Machine vision for feature detection

4.2.1.1 Data acquisition

Foam replacement structures were prepared by first mixing polydimethyl siloxane (Dowsil SE 1700) with 2 wt% fumed silica (Aerosil R 8200) in a Thinky planetary mixer in three intervals of 10 minutes with cooling time in-between to prevent overheating. The ink was then loaded into a syringe and centrifuged for one minute at 3000 rpm to removed trapped air. To print, the ink is then extruded using a Nordson Ultimus I pneumatic pressure system. The ink is then extruded from the syringe and printed as 40x40 mm^2 (length and width) face centered tetragonal lattice structures (**Error! Reference source not found.**). The lattice structures were then cut into 30x30 mm^2 (length and width) structures. The cross-section was then analyzed and imaged through a Keyence VH-ZST (Osaka, Japan) optical microscope.

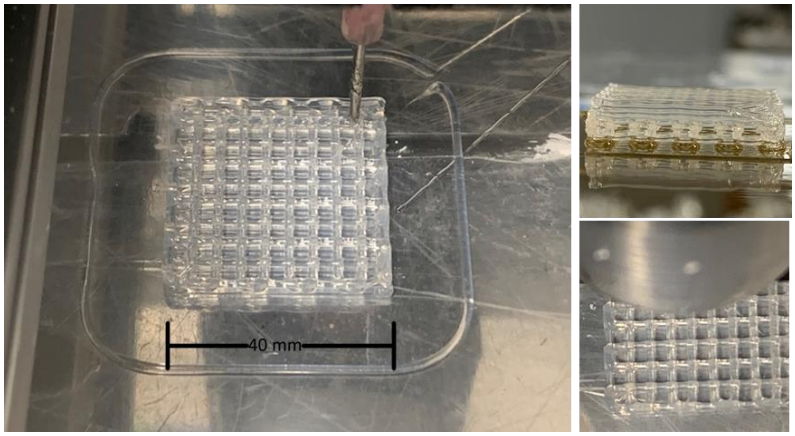

Figure 4.2.1.1: 3D printed foam replacement structures through direct write AM.

4.2.1.2 Automated unit conversion

The purpose of the automated unit converter algorithm is to scale pixel value of to their respective SI units regardless of the scale used by the microscope or magnification. The unit

converter employs an optical character recognizer to read the scale and units located at the bottom of the raw microscope images. By decomposing the text, the scale is stored as an integer value while the units are stored as a string that is associated with a multiplier (e.g., nm = 10^{-9}). Through the use of Hough's Line Transform algorithm, the length of the scale bar is measured in pixel units. Through proportionality, a scaling factor is calculated from the scale integer and the scale bar size. If working with different magnifications or scale bars, the unit associated multiplier is used to keep all measurements on common scales.

4.2.1.3 Feature calculations

Identification of the filament diameter is done through Hough's Circle Transform which outputs the center coordinates and radius for each detected circle. The location of the circles are then used to identify the filament spacing by measuring the distance between horizontally aligned circles. The number of layers were calculated by measuring the number of circles in a column and adding them to the number of lines detected in a column divided by two. This allows for accurate calculation of the number of layers even in the case of sagging.

4.2.2 Machine learning for property prediction of lattice structures

Due to the complex nature of the information that needs to be predicted from the features of the printed lattice structures, an artificial neural network (ANN) was used to fit the prediction model. The ANN comprised of a three-node input layer, a 500-node single hidden layer, and 400-node output layer. The nodes on the input layer were for the filament diameter, the filament spacing, and the number of layers calculated by the by the machine vision algorithm. The 400 layers of the output layer represent the 200 X-coordinates and 200 Y-coordinates on a stress-strain curve. Only a single hidden layer with 500 nodes was used.

The ANN was designed to replicate the results obtained by Roach et al.[45] and trained with the same data set through back propagation and mean squared error (MSE) for gradient decent optimization. Various activation functions for the hidden layer were tested to attempt to replicate the results and the sigmoid activation function was found to best approximate the MSE reported. The training data set consisted of 756 replications for which 80% was used for training, 10% for validation, and 10% for testing. Using 3000 epochs, or iterations, for training, the model reached an MSE value of ~0.1 as reported by Roach et al. [45]

4.3 MACHINE VISION FOR MICROSTRUCTURE ANALYSIS IN SYNTACTIC FOAMS

4.3.1 Syntactic foams

4.3.1.1 Materials, synthesis, and fabrication

The syntactic foams used to train and test the machine vision algorithm were prepared in accordance to Hassan et al.[123]. Bismalemide (BMI) powder was obtained Imitec Inc. (New York, United States). Carbon micro balloons (CMB) with a 5-30 μm diameter particle size distribution and 2.3 μm wall thickness were kindly provided by Honeywell (New Jersey, United States). A Gilson SS-150 sieve shaker from Hogentogler (Maryland, United States) was used to sieve the BMI powder to obtain a 20-80 μm dispersion. The BMI powder was then blended with 10 vol% of CMBs for laser absorbality from the selective laser sintering (SLS) printer and printed with a Sinterit Lisa 3D printer from 3D Herndon (Virginia, United States). The printed BMI/CMB green bodies were then fully cured in an oven at 250 °C for 4 hours.

4.3.1.2 Material characterization

Images of the surface of the syntactic foams were obtained using a Thermo Scientific (Massachusetts, United States) Phenom ProX scanning electron microscope at 15 kV accelerating voltage with a backscatter electron detector. The BMI syntactic foams were first

polished and air blasted for clarity during imaging. Multiple images were obtained from each side of the rectangular prism geometry at several locations.

4.3.2 Algorithm

The machine vision/machine learning algorithm is shown in Figure 4.3.2: Schematic of machine vision and machine learning algorithm and flow. The algorithm takes raw scanning electron micrographs as input and processes the text and visual information separately. The visual information is then segmented through the use of a STARDIST algorithm and characterized into feature to serve as input for the machine learning model. The text information is used to maintain a common scale regardless of magnification used in the imaging process.

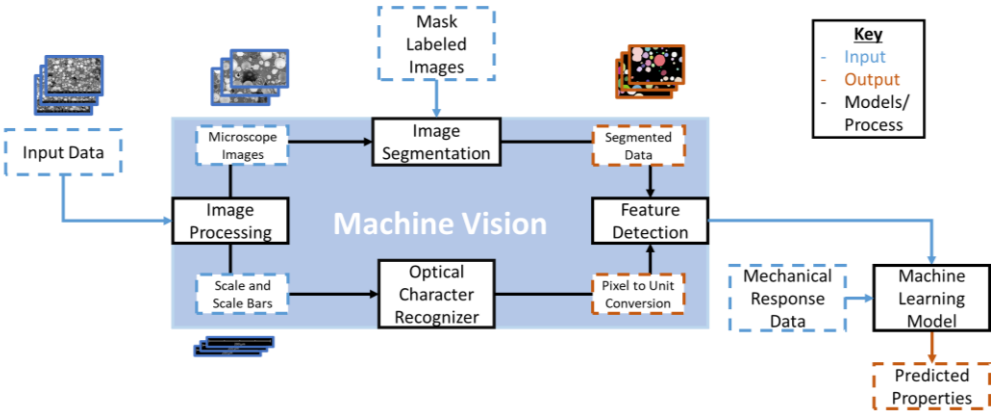

Figure 4.3.2: Schematic of machine vision and machine learning algorithm and flow.

4.3.3 Machine vision for feature detection

4.3.3.1 Data processing

Raw scanning electron microscope images are separated into three parts, the visual image, the scale bar, and scale. The scale bar and scale are processed using an optical character recognizer through the same algorithm presented in section *4.2.1.2 Automated unit conversion*. The visual image is then scaled down by 50% for faster processing without affecting the detectable boundaries. After, the image is cropped in 13 images formed from a 3x3 matric and

the 4-image intersection as shown in Figure 4.3.3.1: Image processing of (left) scanning electron micrograph into (right) smaller crops at lower resolution. These images are exported as .tif files for labeling of training data ground truth.

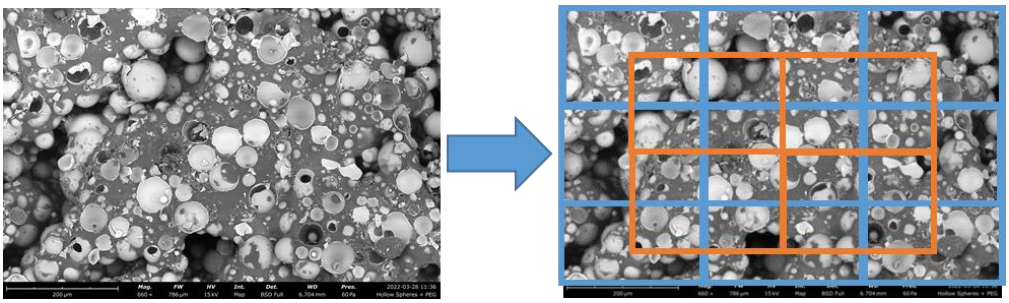

Figure 4.3.3.1: Image processing of (left) scanning electron micrograph into (right) smaller crops at lower resolution.

The training data set was created by manually labeling the CMB shells with the use of ImageJ and the Labkit plugin. The ground truth labels were also exported as .tif files and consisted of 533 image and label pairs.

4.3.3.2 Image segmentation through star-convex polygons

Image segmentation for the detection of CMBs in the 3D printed syntactic foams was done using the STARDIST detection method developed by Schmidt et al. to detect cells[122]. The STARDIST method is trained to densely predict the distance to object boundaries along a fixed set of rays and object probabilities with then produce a set of candidate polygons from an input image. To avoid the detection of an object multiple times, the method employs a non-maximum suppression to obtain the final results, where boxes with low confidence are suppressed by boxes of higher confidence, if they substantially overlap[122].

The first step to evaluate the number of rays the star-convex polygons required for an accurate reconstruction of the ground truth. Figure 4.3.3.2.1: Reconstruction of the ground truth label using number of rays equal to 2^n. shows the reconstruction of the labeled CMBs using a set of rays equal to 2^n where n ranged from 2 to 7. To quantitively determine the minimum number

of rays needed (Figure 4.3.3.2.2: Intersection over union scores of for the reconstruction of the ground truth with varying number of rays.), the mean intersection over union for the input image was calculated, where a score higher than 0.8 is desired. From this study, a minimum number of 16 rays was needed for the accurate reconstruction of the labeled CMBs. For training, the default number of 32 rays was used.

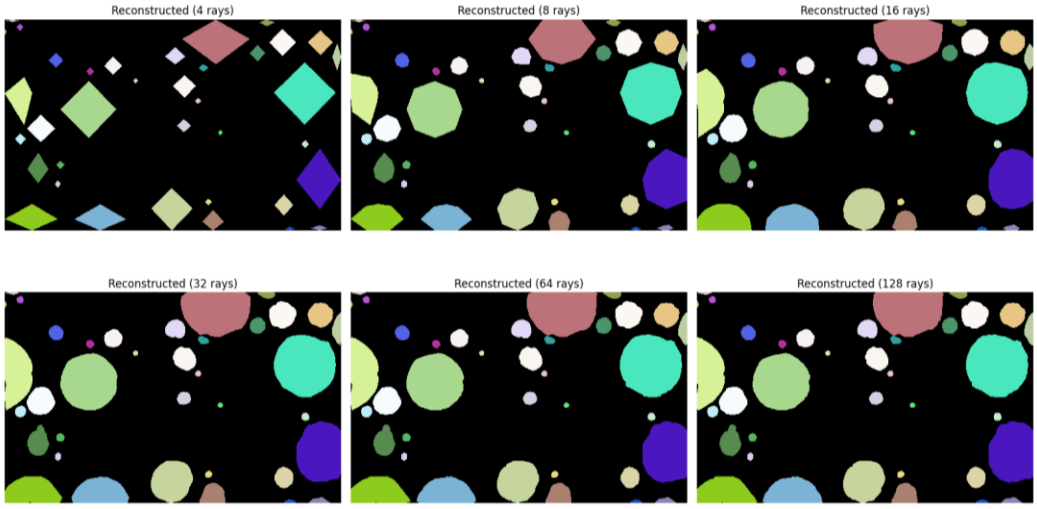

Figure 4.3.3.2.1: Reconstruction of the ground truth label using number of rays equal to 2^n.

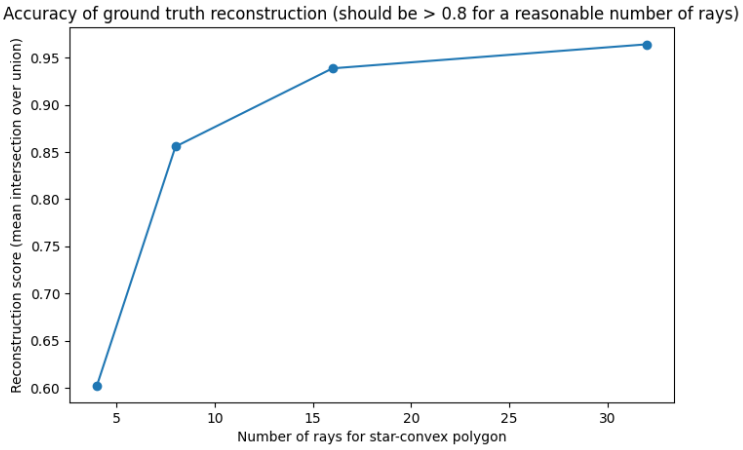

Figure 4.3.3.2.2: Intersection over union scores of for the reconstruction of the ground truth with varying number of rays.

The STARDIST model was trained using a 533 image-label pair dataset. The dataset was augmented by applying random rotations, flips, and intensity changes, in vain of something that

could be obtained from a microscope image. The performance of the detection from the trained STARDIST model was evaluated by measuring the how well the predicted objects overlapped with the ground truth labels. In Figure 4.3.3.2.3: Performance of STARDIST model based on various metrics with respect to intersection over union threshold.various performance were used to evaluate the performance of the model at various intersection over union thresholds (τ). Based on precision and recall scores, bellow $\tau = 0.5$ the model does a fair job at detecting a large portion of the CMB particles. From the test data (Figure 4.3.3.2.4: Comparison of (left) input vs predicted labeling. Red circles highlight features predicted labeling was unable to capture.), however, it can be noted which particle the model has a difficult time detecting. Because the model was not trained sufficiently with labeled small particles, it is unable to distinguish these from noise introduced in the training dataset as debris and dust. For a more accurate detection of the entirety of the CMB dispersion in the BMI matrix, obtaining a larger dataset containing a good portion of small sized CMBs is highly advised.

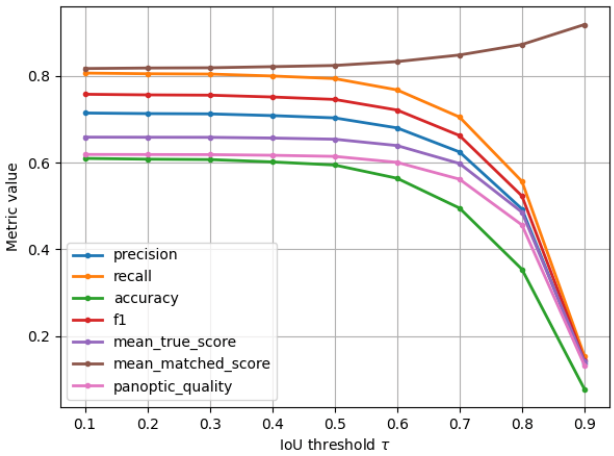

Figure 4.3.3.2.3: Performance of STARDIST model based on various metrics with respect to intersection over union threshold.

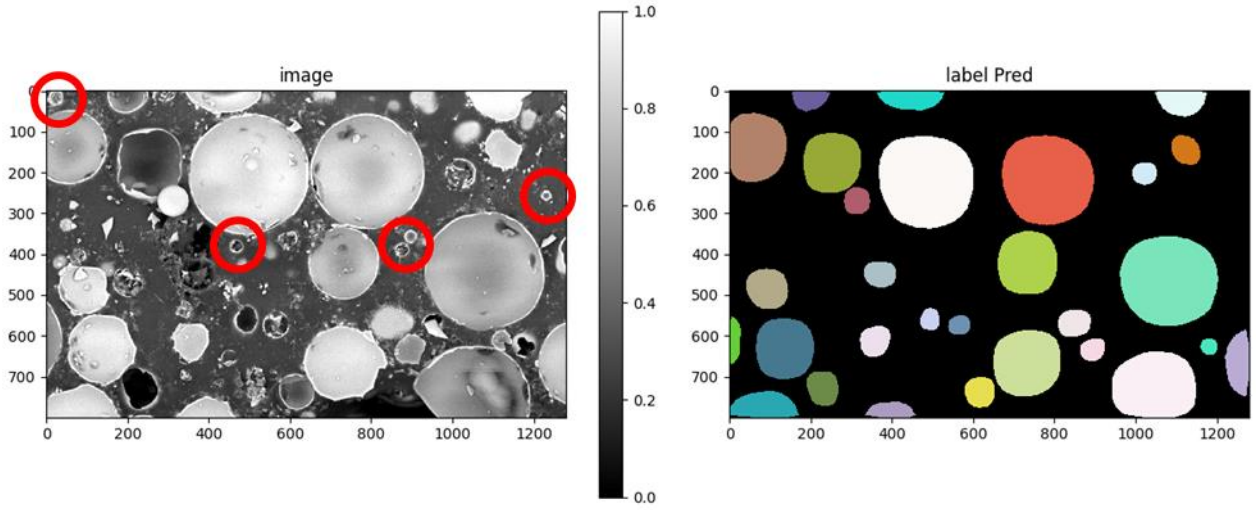

Figure 4.3.3.2.4: Comparison of (left) input vs predicted labeling. Red circles highlight features predicted labeling was unable to capture.

4.3.3.3 Generation of attributes for machine learning

After training, the STARDIST model was used to estimate the particle size distribution of the CMB in the BMI matrix as shown in Figure 4.3.3.3: Particle size distribution and mean particle dimensions of test sample image processed with trained STARDIST model. Since each particle is uniquely labeled, the are that each particle occupies can be calculated through the summation of same valued pixels for every unique instance. By using the conversion factor obtained through the automatic unit conversion sequence, the area of the particles was obtained in SI units. With the assumption that all of the detected particles can be represented by perfect circles, the diameter of the particles can be estimated. The particle size distribution with a pre-determined number of bins can then be used as an input for a machine learning model.

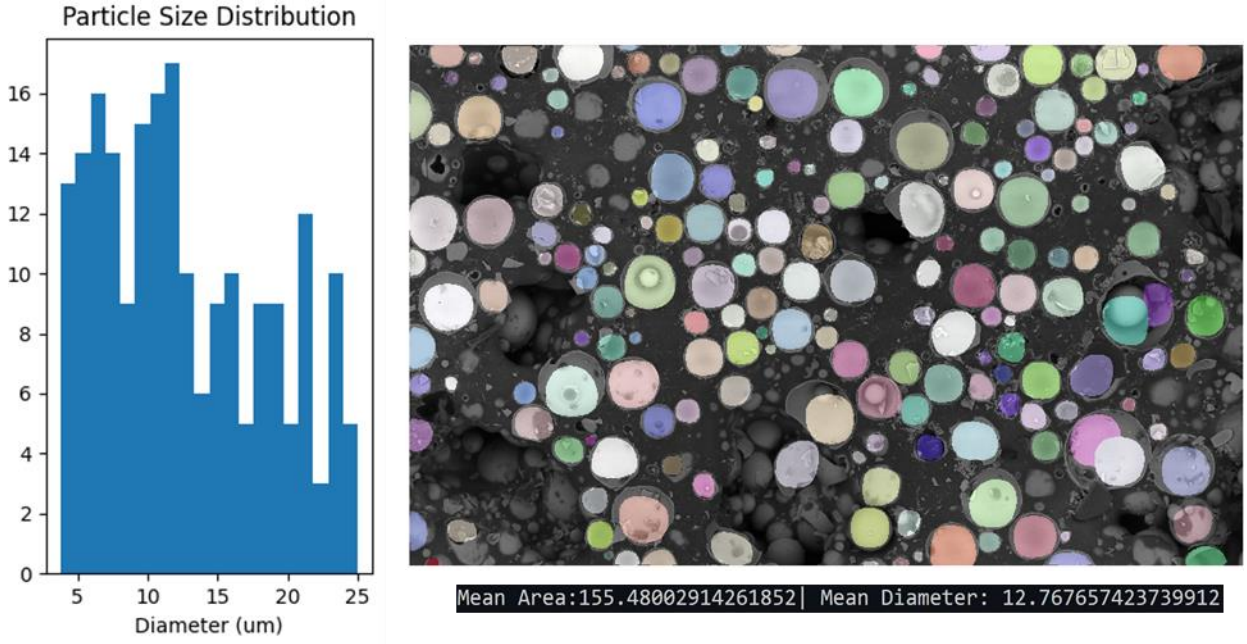

Figure 4.3.3.3: Particle size distribution and mean particle dimensions of test sample image processed with trained STARDIST model.

4.4 CONCLUSION

The capabilities of machine vision for characterization of lattice and syntactic foam structures were demonstrated through two projects. In the first project, machine vision and machine learning for lattice structures, the results from literature were recreated. Through the use of basic computer vision techniques such as Hough's Line and Circle Transforms, the filament diameter, filament spacing, and number of layers were identified from microscope images of silicone lattice structures. This information was then fed into a machine learning model that was validated using a dataset obtained by the literature source we attempted to replicate, obtaining similar results. This project gave us the confidence to further our efforts with syntactic foams.

Due to the more complex nature of in the microstructure of syntactic foams, in comparison to the microstructure of lattice structures, a more robust machine vision method was necessary. Through STARDIST, scanning electron micrographs of the polished surface of bismalemide (BMI)- carbon micro balloons (CMB) syntactic foams were segmented to uniquely

label CMBs on a planar axis of selective laser sintering printed parts. With this information, features such as the particle size distribution were calculated. The trained STARDIST model shows potential for the automatic characterization of syntactic foam microstructures to assist in the generation of data to train machine learning models for property prediction and effectively reduce time by not having to manually extract information from micrographs.

References

[1] J.E. Regis, A. Renteria, S.E. Hall, M.S. Hassan, C. Marquez and Y. Lin, *Recent Trends and Innovation in Additive Manufacturing of Soft Functional Materials*, Materials 14 (2021), pp. 4521.

[2] S. Guessasma, W. Zhang, J. Zhu, S. Belhabib and H. Nouri, *Challenges of additive manufacturing technologies from an optimisation perspective*, Int. J. Simul. Multidiscip. Des. Optim. 6 (2015), pp. A9.

[3] K.S. Novoselov, A.K. Geim, S.V. Morozov, D. Jiang, Y. Zhang, S.V. Dubonos et al., *Electric Field Effect in Atomically Thin Carbon Films*, Science 306 (2004), pp. 666–669.

[4] D.G. Papageorgiou, I.A. Kinloch and R.J. Young, *Mechanical properties of graphene and graphene-based nanocomposites*, Prog. Mater. Sci. 90 (2017), pp. 75–127.

[5] A.A. Balandin, S. Ghosh, W. Bao, I. Calizo, D. Teweldebrhan, F. Miao et al., *Superior Thermal Conductivity of Single-Layer Graphene*, Nano Lett. 8 (2008), pp. 902–907.

[6] K.I. Bolotin, K.J. Sikes, Z. Jiang, M. Klima, G. Fudenberg, J. Hone et al., *Ultrahigh electron mobility in suspended graphene*, Solid State Commun. 146 (2008), pp. 351–355.

[7] R. Atif, I. Shyha and F. Inam, *Mechanical, Thermal, and Electrical Properties of Graphene-Epoxy Nanocomposites—A Review*, Polymers 8 (2016), pp. 281.

[8] Y. Li, Z. Feng, L. Huang, K. Essa, E. Bilotti, H. Zhang et al., *Additive manufacturing high performance graphene-based composites: A review*, Compos. Part Appl. Sci. Manuf. 124 (2019), pp. 105483.

[9] A. Mehmood, N.M. Mubarak, M. Khalid, R. Walvekar, E.C. Abdullah, M.T.H. Siddiqui et al., *Graphene based nanomaterials for strain sensor application—a review*, J. Environ. Chem. Eng. 8 (2020), pp. 103743.

[10] A. Nag, A. Mitra and S.C. Mukhopadhyay, *Graphene and its sensor-based applications: A review*, Sens. Actuators Phys. 270 (2018), pp. 177–194.

[11] Q. Wang and B. Arash, *A review on applications of carbon nanotubes and graphenes as nano-resonator sensors*, Comput. Mater. Sci. 82 (2014), pp. 350–360.

[12] F. Torrisi and T. Carey, *Graphene, related two-dimensional crystals and hybrid systems for printed and wearable electronics*, Nano Today 23 (2018), pp. 73–96.

[13] T.S. Tran, N.K. Dutta and N.R. Choudhury, *Graphene inks for printed flexible electronics: Graphene dispersions, ink formulations, printing techniques and applications*, Adv. Colloid Interface Sci. 261 (2018), pp. 41–61.

[14] W. Lv, Z. Li, Y. Deng, Q.-H. Yang and F. Kang, *Graphene-based materials for electrochemical energy storage devices: Opportunities and challenges*, Energy Storage Mater. 2 (2016), pp. 107–138.

[15] H. Sun, L. Mei, J. Liang, Z. Zhao, C. Lee, H. Fei et al., *Three-dimensional holey-graphene/niobia composite architectures for ultrahigh-rate energy storage*, Science 356 (2017), pp. 599–604.

[16] W. Hooch Antink, Y. Choi, K. Seong, J.M. Kim and Y. Piao, *Recent Progress in Porous Graphene and Reduced Graphene Oxide-Based Nanomaterials for Electrochemical Energy Storage Devices*, Adv. Mater. Interfaces 5 (2018), pp. 1701212.

[17] L.A. Falkovsky, *Optical properties of graphene*, J. Phys. Conf. Ser. 129 (2008), pp. 012004.

[18] S.-E. Zhu, S. Yuan and G.C.A.M. Janssen, *Optical transmittance of multilayer graphene*, EPL Europhys. Lett. 108 (2014), pp. 17007.

[19] Y. Zhu, S. Murali, W. Cai, X. Li, J.W. Suk, J.R. Potts et al., *Graphene and Graphene Oxide: Synthesis, Properties, and Applications*, Adv. Mater. 22 (2010), pp. 3906–3924.

[20] A. Altuntepe, A. Seyhan and R. Zan, *Graphene for Si-based solar cells*, J. Mol. Struct. 1200 (2020), pp. 127055.

[21] P.S. Chandrasekhar, A. Dubey and Q. Qiao, *High efficiency perovskite solar cells using nitrogen-doped graphene/ZnO nanorod composite as an electron transport layer*, Sol. Energy 197 (2020), pp. 78–83.

[22] R. C. Sinclair, J. L. Suter and P. V. Coveney, *Micromechanical exfoliation of graphene on the atomistic scale*, Phys. Chem. Chem. Phys. 21 (2019), pp. 5716–5722.

[23] E. Gao, S.-Z. Lin, Z. Qin, M.J. Buehler, X.-Q. Feng and Z. Xu, *Mechanical exfoliation of two-dimensional materials*, J. Mech. Phys. Solids 115 (2018), pp. 248–262.

[24] M. Yi and Z. Shen, *A review on mechanical exfoliation for the scalable production of graphene*, J. Mater. Chem. A 3 (2015), pp. 11700–11715.

[25] Z.-Y. Juang, C.-Y. Wu, A.-Y. Lu, C.-Y. Su, K.-C. Leou, F.-R. Chen et al., *Graphene synthesis by chemical vapor deposition and transfer by a roll-to-roll process*, Carbon 48 (2010), pp. 3169–3174.

[26] X. Li, L. Colombo and R.S. Ruoff, *Synthesis of Graphene Films on Copper Foils by Chemical Vapor Deposition*, Adv. Mater. 28 (2016), pp. 6247–6252.

[27] R. Muñoz and C. Gómez-Aleixandre, *Review of CVD Synthesis of Graphene*, Chem. Vap. Depos. 19 (2013), pp. 297–322.

[28] A. Amiri, M. Naraghi, G. Ahmadi, M. Soleymaniha and M. Shanbedi, *A review on liquid-phase exfoliation for scalable production of pure graphene, wrinkled, crumpled and functionalized graphene and challenges*, FlatChem 8 (2018), pp. 40–71.

[29] X. Gu, Y. Zhao, K. Sun, C.L.Z. Vieira, Z. Jia, C. Cui et al., *Method of ultrasound-assisted liquid-phase exfoliation to prepare graphene*, Ultrason. Sonochem. 58 (2019), pp. 104630.

[30] Y. Hernandez, V. Nicolosi, M. Lotya, F.M. Blighe, Z. Sun, S. De et al., *High-yield production of graphene by liquid-phase exfoliation of graphite*, Nat. Nanotechnol. 3 (2008), pp. 563–568.

[31] H. Guo, R. Lv and S. Bai, *Recent advances on 3D printing graphene-based composites*, Nano Mater. Sci. 1 (2019), pp. 101–115.

[32] N. Zheng, Y. Xu, Q. Zhao and T. Xie, *Dynamic Covalent Polymer Networks: A Molecular Platform for Designing Functions beyond Chemical Recycling and Self-Healing*, Chem. Rev. 121 (2021), pp. 1716–1745.

[33] L.M. Cox, Z. Li, N. Sowan, D. Nair, J. Xiao, C.N. Bowman et al., *Reconfigurable surface patterns on covalent adaptive network polymers using nanoimprint lithography*, Polymer 55 (2014), pp. 5933–5937.

[34] M. Podgórski, B.D. Fairbanks, B.E. Kirkpatrick, M. McBride, A. Martinez, A. Dobson et al., *Toward Stimuli-Responsive Dynamic Thermosets through Continuous Development and Improvements in Covalent Adaptable Networks (CANs)*, Adv. Mater. 32 (2020), pp. 1906876.

[35] K. Yang, J.C. Grant, P. Lamey, A. Joshi-Imre, B.R. Lund, R.A. Smaldone et al., *Diels–Alder Reversible Thermoset 3D Printing: Isotropic Thermoset Polymers via Fused Filament Fabrication*, Adv. Funct. Mater. 27 (2017), pp. 1700318.

[36] M. Nadgorny, Z. Xiao and L. A. Connal, *2D and 3D-printing of self-healing gels: design and extrusion of self-rolling objects*, Mol. Syst. Des. Eng. 2 (2017), pp. 283–292.

[37] B. Zhang, K. Kowsari, A. Serjouei, M.L. Dunn and Q. Ge, *Reprocessable thermosets for sustainable three-dimensional printing*, Nat. Commun. 9 (2018), pp. 1831.

[38] Q. Shi, K. Yu, X. Kuang, X. Mu, C. K. Dunn, M. L. Dunn et al., *Recyclable 3D printing of vitrimer epoxy*, Mater. Horiz. 4 (2017), pp. 598–607.

[39] F. Nelli, *Python Data Analytics: Data Analysis and Science Using Pandas, Matplotlib and the Python Programming Language*, Apress, 2015.

[40] Z. Jin, Z. Zhang, K. Demir and G.X. Gu, *Machine Learning for Advanced Additive Manufacturing*, Matter 3 (2020), pp. 1541–1556.

[41] D. Chen, M. Skouras, B. Zhu and W. Matusik, *Computational discovery of extremal microstructure families*, Sci. Adv. 4 pp. eaao7005.

[42] G. X. Gu, C.-T. Chen, D. J. Richmond and M. J. Buehler, *Bioinspired hierarchical composite design using machine learning: simulation, additive manufacturing, and experiment*, Mater. Horiz. 5 (2018), pp. 939–945.

[43] Z. Jin, Z. Zhang and G.X. Gu, *Autonomous in-situ correction of fused deposition modeling printers using computer vision and deep learning*, Manuf. Lett. 22 (2019), pp. 11–15.

[44] L. Scime and J. Beuth, *Anomaly detection and classification in a laser powder bed additive manufacturing process using a trained computer vision algorithm*, Addit. Manuf. 19 (2018), pp. 114–126.

[45] *Utilizing computer vision and artificial intelligence algorithms to predict and design the mechanical compression response of direct ink write 3D printed foam replacement structures | Elsevier Enhanced Reader*. Available at https://reader.elsevier.com/reader/sd/pii/S2214860421001159?token=334F792553D866EC6

00AFF25849B275D5E7ECDCEC52C4405B3AD3847E3ECC284E7FEF2D31CC1DFF9969D5744B5A57B35&originRegion=us-east-1&originCreation=20220118202736.

[46] Y.L. Zhong, Z. Tian, G.P. Simon and D. Li, *Scalable production of graphene via wet chemistry: progress and challenges*, Mater. Today 18 (2015), pp. 73–78.

[47] S. Abdolhosseinzadeh, H. Asgharzadeh and H.S. Kim, *Fast and fully-scalable synthesis of reduced graphene oxide*, Sci. Rep. 5 (2015), pp. 1–7.

[48] X. Zhou and Z. Liu, *A scalable, solution-phase processing route to graphene oxide and graphene ultralarge sheets*, Chem. Commun. 46 (2010), pp. 2611–2613.

[49] K.P. Loh, Q. Bao, G. Eda and M. Chhowalla, *Graphene oxide as a chemically tunable platform for optical applications*, Nat. Chem. 2 (2010), pp. 1015–1024.

[50] Q. Mei, B. Liu, G. Han, R. Liu, M.-Y. Han and Z. Zhang, *Graphene Oxide: From Tunable Structures to Diverse Luminescence Behaviors*, Adv. Sci. 6 (2019), pp. 1900855.

[51] D. R. Dreyer, S. Park, C. W. Bielawski and R. S. Ruoff, *The chemistry of graphene oxide*, Chem. Soc. Rev. 39 (2010), pp. 228–240.

[52] N.I. Zaaba, K.L. Foo, U. Hashim, S.J. Tan, W.-W. Liu and C.H. Voon, *Synthesis of Graphene Oxide using Modified Hummers Method: Solvent Influence*, Procedia Eng. 184 (2017), pp. 469–477.

[53] J. Guerrero-Contreras and F. Caballero-Briones, *Graphene oxide powders with different oxidation degree, prepared by synthesis variations of the Hummers method*, Mater. Chem. Phys. 153 (2015), pp. 209–220.

[54] C. Botas, P. Álvarez, P. Blanco, M. Granda, C. Blanco, R. Santamaría et al., *Graphene materials with different structures prepared from the same graphite by the Hummers and Brodie methods*, Carbon 65 (2013), pp. 156–164.

[55] A. Dideykin, A.E. Aleksenskiy, D. Kirilenko, P. Brunkov, V. Goncharov, M. Baidakova et al., *Monolayer graphene from graphite oxide*, Diam. Relat. Mater. 20 (2011), pp. 105–108.

[56] S. Pei and H.-M. Cheng, *The reduction of graphene oxide*, Carbon 50 (2012), pp. 3210–3228.

[57] C. Kiang Chua and M. Pumera, *Chemical reduction of graphene oxide: a synthetic chemistry viewpoint*, Chem. Soc. Rev. 43 (2014), pp. 291–312.

[58] L. G. Guex, B. Sacchi, K. F. Peuvot, R. L. Andersson, A. M. Pourrahimi, V. Ström et al., *Experimental review: chemical reduction of graphene oxide (GO) to reduced graphene oxide (rGO) by aqueous chemistry*, Nanoscale 9 (2017), pp. 9562–9571.

[59] S. Park, J. An, J.R. Potts, A. Velamakanni, S. Murali and R.S. Ruoff, *Hydrazine-reduction of graphite- and graphene oxide*, Carbon 49 (2011), pp. 3019–3023.

[60] X. Gao, J. Jang and S. Nagase, *Hydrazine and Thermal Reduction of Graphene Oxide: Reaction Mechanisms, Product Structures, and Reaction Design*, J. Phys. Chem. C 114 (2010), pp. 832–842.

[61] M. Khan, A.H. Al-Marri, M. Khan, M.R. Shaik, N. Mohri, S.F. Adil et al., *Green Approach for the Effective Reduction of Graphene Oxide Using Salvadora persica L. Root (Miswak) Extract*, Nanoscale Res. Lett. 10 (2015), pp. 281.

[62] G. Lee and B.S. Kim, *Biological reduction of graphene oxide using plant leaf extracts*, Biotechnol. Prog. 30 (2014), pp. 463–469.

[63] S.B. Maddinedi, B.K. Mandal, R. Vankayala, P. Kalluru and S.R. Pamanji, *Bioinspired reduced graphene oxide nanosheets using Terminalia chebula seeds extract*, Spectrochim. Acta. A. Mol. Biomol. Spectrosc. 145 (2015), pp. 117–124.

[64] S. Gurunathan, J.W. Han, V. Eppakayala and J.-H. Kim, *Microbial reduction of graphene oxide by Escherichia coli: A green chemistry approach*, Colloids Surf. B Biointerfaces 102 (2013), pp. 772–777.

[65] G. Wang, F. Qian, C.W. Saltikov, Y. Jiao and Y. Li, *Microbial reduction of graphene oxide by Shewanella*, Nano Res. 4 (2011), pp. 563–570.

[66] O. Akhavan and E. Ghaderi, *Escherichia coli bacteria reduce graphene oxide to bactericidal graphene in a self-limiting manner*, Carbon 50 (2012), pp. 1853–1860.

[67] B. Li, X. Jin, J. Lin and Z. Chen, *Green reduction of graphene oxide by sugarcane bagasse extract and its application for the removal of cadmium in aqueous solution*, J. Clean. Prod. 189 (2018), pp. 128–134.

[68] C. Guo, B. Book-Newell and J. Irudayaraj, *Protein -directed reduction of graphene oxide and intracellular imaging*, Chem. Commun. 47 (2011), pp. 12658–12660.

[69] Z. Sheng, L. Song, J. Zheng, D. Hu, M. He, M. Zheng et al., *Protein-assisted fabrication of nano-reduced graphene oxide for combined in vivo photoacoustic imaging and photothermal therapy*, Biomaterials 34 (2013), pp. 5236–5243.

[70] J. Kauppila, P. Kunnas, P. Damlin, A. Viinikanoja and C. Kvarnström, *Electrochemical reduction of graphene oxide films in aqueous and organic solutions*, Electrochimica Acta 89 (2013), pp. 84–89.

[71] K.K.H. De Silva, H.-H. Huang, R.K. Joshi and M. Yoshimura, *Chemical reduction of graphene oxide using green reductants*, Carbon 119 (2017), pp. 190–199.

[72] M.J. Fernández-Merino, L. Guardia, J.I. Paredes, S. Villar-Rodil, P. Solís-Fernández, A. Martínez-Alonso et al., *Vitamin C Is an Ideal Substitute for Hydrazine in the Reduction of Graphene Oxide Suspensions*, J. Phys. Chem. C 114 (2010), pp. 6426–6432.

[73] O. Akhavan, E. Ghaderi, S. Aghayee, Y. Fereydooni and A. Talebi, *The use of a glucose-reduced graphene oxide suspension for photothermal cancer therapy*, J. Mater. Chem. 22 (2012), pp. 13773–13781.

[74] Y. Feng, N. Feng and G. Du, *A green reduction of graphene oxide via starch-based materials*, RSC Adv. 3 (2013), pp. 21466–21474.

[75] O. Akhavan, R. Azimirad, H.T. Gholizadeh and F. Ghorbani, *Hydrogen-rich water for green reduction of graphene oxide suspensions*, Int. J. Hydrog. Energy 40 (2015), pp. 5553–5560.

[76] O. Akhavan, E. Ghaderi, E. Abouei, S. Hatamie and E. Ghasemi, *Accelerated differentiation of neural stem cells into neurons on ginseng-reduced graphene oxide sheets*, Carbon 66 (2014), pp. 395–406.

[77] H. Peng, L. Meng, L. Niu and Q. Lu, *Simultaneous Reduction and Surface Functionalization of Graphene Oxide by Natural Cellulose with the Assistance of the Ionic Liquid*, J. Phys. Chem. C 116 (2012), pp. 16294–16299.

[78] P. Khanra, T. Kuila, N.H. Kim, S.H. Bae, D. Yu and J.H. Lee, *Simultaneous bio-functionalization and reduction of graphene oxide by baker's yeast*, Chem. Eng. J. 183 (2012), pp. 526–533.

[79] J. Li, G. Xiao, C. Chen, R. Li and D. Yan, *Superior dispersions of reduced graphene oxide synthesized by using gallic acid as a reductant and stabilizer*, J. Mater. Chem. A 1 (2012), pp. 1481–1487.

[80] P. Chamoli, M. K. Das and K. K. Kar, *Temperature dependence green reduction of graphene oxide by urea*, Adv. Mater. Lett. 8 (2017), pp. 217–222.

[81] O. Akhavan, E. Ghaderi and A. Esfandiar, *Wrapping Bacteria by Graphene Nanosheets for Isolation from Environment, Reactivation by Sonication, and Inactivation by Near-Infrared Irradiation*, J. Phys. Chem. B 115 (2011), pp. 6279–6288.

[82] O. Akhavan and E. Ghaderi, *Photocatalytic Reduction of Graphene Oxide Nanosheets on TiO2 Thin Film for Photoinactivation of Bacteria in Solar Light Irradiation*, J. Phys. Chem. C 113 (2009), pp. 20214–20220.

[83] E.E. Ghadim, N. Rashidi, S. Kimiagar, O. Akhavan, F. Manouchehri and E. Ghaderi, *Pulsed laser irradiation for environment friendly reduction of graphene oxide suspensions*, Appl. Surf. Sci. 301 (2014), pp. 183–188.

[84] W. Chae, M. Kim, D. Kim, J.-H. Park, W. Choi and J. Lee, *Photo-Reduction of Graphene Oxide by Using Photographic Flash-Light*, Sci. Adv. Mater. 10 (2018), pp. 130–133.

[85] Y. Zhou, Q. Bao, L.A.L. Tang, Y. Zhong and K.P. Loh, *Hydrothermal Dehydration for the "Green" Reduction of Exfoliated Graphene Oxide to Graphene and Demonstration of Tunable Optical Limiting Properties*, Chem. Mater. 21 (2009), pp. 2950–2956.

[86] J. Zhang, H. Yang, G. Shen, P. Cheng, J. Zhang and S. Guo, *Reduction of graphene oxide via l - ascorbic acid*, Chem. Commun. 46 (2010), pp. 1112–1114.

[87] A. Abulizi, K. Okitsu and J.-J. Zhu, *Ultrasound assisted reduction of graphene oxide to graphene in l-ascorbic acid aqueous solutions: Kinetics and effects of various factors on the rate of graphene formation*, Ultrason. Sonochem. 21 (2014), pp. 1174–1181.

[88] J. Usaga, D.C. Manns, C.I. Moraru, R.W. Worobo and O.I. Padilla-Zakour, *Ascorbic acid and selected preservatives influence effectiveness of UV treatment of apple juice*, LWT 75 (2017), pp. 9–16.

[89] Hindawi, *Synthesis and Characterization of Graphene Thin Films by Chemical Reduction of Exfoliated and Intercalated Graphite Oxide*. Available at https://www.hindawi.com/journals/jchem/2013/150536/.

[90] V. Dua, S.P. Surwade, S. Ammu, S.R. Agnihotra, S. Jain, K.E. Roberts et al., *All-Organic Vapor Sensor Using Inkjet-Printed Reduced Graphene Oxide*, Angew. Chem. Int. Ed. 49 (2010), pp. 2154–2157.

[91] I. Kanayama, H. Miyaji, H. Takita, E. Nishida, M. Tsuji, B. Fugetsu et al., *Comparative study of bioactivity of collagen scaffolds coated with graphene oxide and reduced graphene oxide*, Int. J. Nanomedicine 9 (2014), pp. 3363–3373.

[92] K. Wang, J. Pang, L. Li, S. Zhou, Y. Li and T. Zhang, *Synthesis of hydrophobic carbon nanotubes/reduced graphene oxide composite films by flash light irradiation*, Front. Chem. Sci. Eng. 12 (2018), pp. 376–382.

[93] F. Zhang, J. Ilavsky, G.G. Long, J.P.G. Quintana, A.J. Allen and P.R. Jemian, *Glassy Carbon as an Absolute Intensity Calibration Standard for Small-Angle Scattering*, Metall. Mater. Trans. A 41 (2010), pp. 1151–1158.

[94] D.M. Moore and R.C. Reynolds, *X-Ray Diffraction and the Identification and Analysis of Clay Minerals.*, Oxford University Press (OUP), 1989.

[95] X. Shen, X. Lin, N. Yousefi, J. Jia and J.-K. Kim, *Wrinkling in graphene sheets and graphene oxide papers*, Carbon 66 (2014), pp. 84–92.

[96] D.A. Dikin, S. Stankovich, E.J. Zimney, R.D. Piner, G.H.B. Dommett, G. Evmenenko et al., *Preparation and characterization of graphene oxide paper*, Nature 448 (2007), pp. 457–460.

[97] B. Lian, S.D. Luca, Y. You, S. Alwarappan, M. Yoshimura, V. Sahajwalla et al., *Extraordinary water adsorption characteristics of graphene oxide*, Chem. Sci. 9 (2018), pp. 5106–5111.

[98] T.N. Blanton and D. Majumdar, *X-ray diffraction characterization of polymer intercalated graphite oxide*, Powder Diffr. 27 (2012), pp. 104–107.

[99] J.B. Thomas, J.H. Yen and K.E. Sharpless, *Characterization of NIST food-matrix standard reference materials for their vitamin C content*, Anal. Bioanal. Chem. 405 (2013), pp. 4539–4548.

[100] K.K.H. De Silva, H.-H. Huang and M. Yoshimura, *Progress of reduction of graphene oxide by ascorbic acid*, Appl. Surf. Sci. 447 (2018), pp. 338–346.

[101] Z. Bo, X. Shuai, S. Mao, H. Yang, J. Qian, J. Chen et al., *Green preparation of reduced graphene oxide for sensing and energy storage applications*, Sci. Rep. 4 (2014), pp. 4684.

[102] J.Y. Chong, B. Wang, C. Mattevi and K. Li, *Dynamic microstructure of graphene oxide membranes and the permeation flux*, J. Membr. Sci. 549 (2018), pp. 385–392.

[103] D.W. Boukhvalov, M.I. Katsnelson and Y.-W. Son, *Origin of Anomalous Water Permeation through Graphene Oxide Membrane*, Nano Lett. 13 (2013), pp. 3930–3935.

[104] R.R. Nair, H.A. Wu, P.N. Jayaram, I.V. Grigorieva and A.K. Geim, *Unimpeded Permeation of Water Through Helium-Leak–Tight Graphene-Based Membranes*, Science 335 (2012), pp. 442–444.

[105] H. Korhonen, L.H. Sinh, N.D. Luong, P. Lehtinen, T. Verho, J. Partanen et al., *Fabrication of graphene-based 3D structures by stereolithography*, Phys. Status Solidi A 213 (2016), pp. 982–985.

[106] S.-H. Go, H. Kim, J. Yu, N.-H. You, B.-C. Ku and Y.-K. Kim, *Synergistic effect of UV and l-ascorbic acid on the reduction of graphene oxide: Reduction kinetics and quantum chemical simulations*, Solid State Sci. 84 (2018), pp. 120–125.

[107] J. Regis, S. Vargas, A. Irigoyen, E. Bramasco-Rivera, J.L. Bañuelos, L.C. Delfin et al., *Near-UV light assisted green reduction of graphene oxide films through l-ascorbic acid*, Int. J. Smart Nano Mater. 12 (2021), pp. 20–35.

[108] W. Denissen, J. M. Winne and F.E.D. Prez, *Vitrimers: permanent organic networks with glass-like fluidity*, Chem. Sci. 7 (2016), pp. 30–38.

[109] D. Montarnal, M. Capelot, F. Tournilhac and L. Leibler, *Silica-Like Malleable Materials from Permanent Organic Networks*, Science 334 (2011), pp. 965–968.

[110] A. Ruiz de Luzuriaga, G. Solera, I. Azcarate-Ascasua, V. Boucher, H.-J. Grande and A. Rekondo, *Chemical control of the aromatic disulfide exchange kinetics for tailor-made epoxy vitrimers*, Polymer 239 (2022), pp. 124457.

[111] A.R. de Luzuriaga, J.M. Matxain, F. Ruipérez, R. Martin, J.M. Asua, G. Cabañero et al., *Transient mechanochromism in epoxy vitrimer composites containing aromatic disulfide crosslinks*, J. Mater. Chem. C 4 (2016), pp. 6220–6223.

[112] E.M. Stocking and R.M. Williams, *Chemistry and Biology of Biosynthetic Diels–Alder Reactions*, Angew. Chem. Int. Ed. 42 (2003), pp. 3078–3115.

[113] M. E. Belowich and J. Fraser Stoddart, *Dynamic imine chemistry*, Chem. Soc. Rev. 41 (2012), pp. 2003–2024.

[114] S. Kitagawa and R. Matsuda, *Chemistry of coordination space of porous coordination polymers*, Coord. Chem. Rev. 251 (2007), pp. 2490–2509.

[115] B. Krishnakumar, R.V.S. Prasanna Sanka, W.H. Binder, C. Park, J. Jung, V. Parthasarthy et al., *Catalyst free self-healable vitrimer/graphene oxide nanocomposites*, Compos. Part B Eng. 184 (2020), pp. 107647.

[116] J. Ishibashi, Y. Fang and J. Kalow, *Exploiting block copolymer phase segregation to tune vitrimer properties*, (2021), .

[117] H. Alhumade, H. Rezk, A.M. Nassef and M. Al-Dhaifallah, *Fuzzy Logic Based-Modeling and Parameter Optimization for Improving the Corrosion Protection of Stainless Steel 304 by Epoxy-Graphene Composite*, IEEE Access 7 (2019), pp. 100899–100909.

[118] F. Ji, Y. Zhou and Y. Yang, *Tailoring the structure and properties of epoxy–polyurea vitrimers via controllable network reconfiguration*, J. Mater. Chem. A 9 (2021), pp. 7172–7179.

[119] G.I. Peterson, M.B. Larsen, M.A. Ganter, D.W. Storti and A.J. Boydston, *3D-Printed Mechanochromic Materials*, ACS Appl. Mater. Interfaces 7 (2015), pp. 577–583.

[120] D.J. Roach, A. Rohskopf, C.M. Hamel, W.D. Reinholtz, R. Bernstein, H.J. Qi et al., *Utilizing computer vision and artificial intelligence algorithms to predict and design the mechanical compression response of direct ink write 3D printed foam replacement structures*, Addit. Manuf. 41 (2021), pp. 101950.

[121] L.O. Afolabi, Z.M. Ariff, S.F.S. Hashim, T. Alomayri, S. Mahzan, K.-A. Kamarudin et al., *Syntactic foams formulations, production techniques, and industry applications: a review*, J. Mater. Res. Technol. 9 (2020), pp. 10698–10718.

[122] U. Schmidt, M. Weigert, C. Broaddus and G. Myers, Cell Detection with Star-Convex Polygons, in Medical Image Computing and Computer Assisted Intervention – MICCAI 2018, 2018, pp. 265–273.

[123] M.S. Hassan, K.M.M. Billah, S.E. Hall, S. Sepulveda, J.E. Regis, C. Marquez et al., *Selective Laser Sintering of High-Temperature Thermoset Polymer*, J. Compos. Sci. 6 (2022), pp. 41.

Vita

Jaime Eduardo Regis was born and raised in El Paso Texas. After graduating valedictorian from Del Valle High School in 2014, Jaime enrolled in the Mechanical Engineering program at the University of Texas at El Paso (UTEP) in pursuit of his Bachelor of Science degree as a first-generation college student.

In Summer 2017, Jaime took part in a ten-week summer internship with the Army High Performance Computing Research Center at Stanford University where he became acquainted with computational fluid dynamics and performed parametric studies on adaptive mesh refinement. After, he joined the Smart Materials Processing Lab at the University of Texas at El Paso where he worked on the synthesis and fabrication of functional composites with self-sensing and self-healing capabilities through additive manufacturing. After presenting his research at the Materials Research Outreach Program at the University of California Santa Barbara he was offered a summer internship with the Future Leaders in Advanced Materials at the same institution, where he developed a program to automate and parallelize nanomechanical testing of materials while imaging the test inside a scanning electron microscope.

Jaime graduated from the University of Texas at El Paso with his Bachelor of Science in Mechanical Engineering honors in 2018 with honors and proceeded to pursue his Doctor of Philosophy degree in Mechanical Engineering. He furthered his professional development through internships with Los Alamos National Labs and Kansas City National Security Campus. During his time as a doctoral student, Jaime published two first-authored journal publication and co-authored 11 additional publications.

Contact Information: jeregis@miners.utep.edu